Journal of Hydrology 598 (2021) 126224

Contents lists available at ScienceDirect

Journal of Hydrology

journal homepage: www.elsevier.com/locate/jhydrol

Research papers

Estimation of Long-duration Maximum Precipitation during a winter season for large basins dominated by Atmospheric Rivers using a Numerical Weather Model

Yusuke Hiraga [a,*], Yoshihiko Iseri [a], Michael D. Warner [b], Chris D. Frans [b], Angela M. Duren [c], John F. England [d], M. Levent Kavvas [a]

[a] Department of Civil and Environmental Engineering, University of California, Davis, Davis, CA, United States
[b] Seattle District, U.S. Army Corps of Engineers, Seattle, WA, United States
[c] Northwest Division, U.S. Army Corps of Engineers, Portland, OR, United States
[d] Risk Management Center, U.S. Army Corps of Engineers, Lakewood, CO, United States

ARTICLE INFO

This manuscript was handled by Andras Bardossy, Editor-in-Chief, with the assistance of Uwe Haberlandt, Associate Editor

Keywords:
Probable maximum precipitation (PMP)
Regional climate model (RCM)
Weather Research and Forecasting Model (WRF)
Integrated water vapor transport (IVT)
Pacific Northwest (PNW)
Columbia River Basin (CRB)

ABSTRACT

The Probable Maximum Precipitation (PMP) estimation for long durations during winter and spring seasons is important to develop the Probable Maximum Flood for snowmelt-driven regions since extreme floods are often characterized by snow-accumulation and snowmelt processes rather than by a single rainstorm event. Although several studies have estimated the PMP for a single storm duration, little attention has been given to the PMP estimation for long durations on the order of several months. This study proposes a new framework using a numerical weather model (NWM) to estimate the long-duration Maximum Precipitation (MP) during the winter season, which is the first part of a two-part effort to develop the PMP during the winter and spring seasons. As a demonstrative case, we estimate the MP for the 6-month winter period (October to March) for the drainage areas of Bonneville Dam (621,600 km^2) and Libby Dam (23,270 km^2) in the Columbia River Basin dominated by atmospheric rivers (ARs). In the proposed framework, the historical AR events are identified based on the integrated water vapor transport thresholds used in the AR category scale. The precipitation depths during the identified AR events are then maximized by simultaneously optimizing the AR position and its atmospheric moisture. Finally, the design precipitation sequence is formed by substituting each historical AR event with the corresponding maximized AR event, acting as the basis of long-duration MP. As a result, the maximum 6-month winter period accumulated basin-average precipitation depths: long-duration MP, for the drainage areas of Bonneville Dam and Libby Dam, are estimated to be 961.0 mm and 1101.7 mm, respectively. To the authors' knowledge, this is the first study estimating the MP for long durations on the order of several months and for very large basins (above 100,000 km^2) by using the NWM-based approach.

1. Introduction

The Probable Maximum Precipitation (PMP) concept has been widely used as a design basis to estimate the Probable Maximum Flood (PMF) (WMO, 2009). The PMP is defined as the theoretical maximum precipitation for a given duration under possible meteorological conditions (WMO, 2009). Since the PMP is a key parameter for estimating PMF, the accurate estimation of the PMP is of considerable importance for the design and risk assessment of the potential failure of hydraulic structures. Traditional approaches to estimate the PMP can be classified mainly into two categories: The statistical approach and the storm maximization approach.

The statistical approach is usually referred to as Hershfield's method (Hershfield, 1961, 1965), which is based on the general frequency equation proposed by Chow (1951). Since Hershfield's method requires only observed annual maximum daily precipitation data, it has been applied in many regions of the world (Casas et al., 2008; Desa M et al., 2001; Rakhecha et al., 1992; Rezacova et al., 2005; Sarkar and Maity, 2020a, 2020b; Sherif et al., 2014; Tajbakhsh and Al-Ansari, 2019). Several problematic issues associated with Hershfield's method,

* Corresponding author at: One Shields Avenue, Davis, CA 95616, USA.
E-mail address: yhiraga@ucdavis.edu (Y. Hiraga).

https://doi.org/10.1016/j.jhydrol.2021.126224
Received 28 October 2020; Received in revised form 9 February 2021; Accepted 15 March 2021
Available online 19 March 2021
0022-1694/© 2021 The Author(s). Published by Elsevier B.V. This is an open access article under the CC BY-NC-ND license (http://creativecommons.org/licenses/by-nc-nd/4.0/).

however, have been reported. For instance, Koutsoyiannis (1999) argued Hershfield's method might not provide the physical upper limit of precipitation but rather rainfall with a given significant return period. Nobilis et al. (1991) argued that Hershfield's method is inadequate for observed precipitation series with outliers. Furthermore, Hershfield's method may not produce realistic spatial variations of PMP since it yields only point values of PMP where the observed precipitation data are available and thus requires area-reduction curves to adjust the point values to areas of various size (WMO, 2009).

In the storm maximization approach, the PMP is determined by the transposition and moisture maximization of historical severe rainstorms (Hansen et al., 1994). This approach maximizes the historical storms by multiplying them by the ratio of PW_{max}/PW, where PW is actual precipitable water in the atmosphere, and PW_{max} is maximum precipitable water estimated by maximum daily dew point temperature of the corresponding month (WMO, 2009). Hence, the storm maximization approach lies in the assumption that precipitation depth and PW are linearly related. The storm maximization approach has been a widely recognized technique for the PMP estimation, especially in North America (Beauchamp et al., 2013; Hansen et al., 1994; Rouhani and Leconte, 2016; Rousseau et al., 2014). The limitations of the storm maximization approach, however, have been discussed in several studies as it is insufficiently grounded in physics. Several studies showed, using numerical weather models, that the linear relationship between PW and precipitation depth might not necessarily hold in reality (Abbs, 1999; Rastogi et al., 2017; Zhao et al., 1997). Chen and Bradley (2006) found that the pseudo-adiabatic profile assumption, which is used to calculate actual PW based on the surface dew point temperature or sea surface temperature, could overestimate PW. Moreover, PMP estimation under the hypothesis of stationarity is not valid under changing precipitation patterns led by climate change (Ben Alaya et al., 2020; Chen et al., 2017; Cheng and Aghakouchak, 2014; Gao et al., 2016; Ishida et al., 2018a, 2018b; Kunkel et al., 2013).

Furthermore, the two traditional methods mentioned above have limitations regarding the spatial extent of the PMP estimation. The statistical approach is mainly applicable for watersheds with a drainage area less than 1000 km^2 (390 sq mi) (WMO, 1986; 2009). The storm maximization approach, referred to as the storm separation method in HMRs, is traditionally limited to areas of 25,900 km^2 (10,000 sq mi) and durations of 72 h, or less for generalized PMP estimates (Hansen et al., 1982, 1994). However, the total drainage area of a dam located at the most downstream of many upstream dam systems, such as the drainage area of Bonneville Dam in the Columbia River Basin (CRB), can be much larger than 25,900 km^2 (10,000 sq mi). The traditional approaches cannot be applied directly to the PMP estimation for such large drainage areas. Moreover, even though the meteorological/hydrological conditions of multiple dams are mutually dependent, these traditional approaches need to estimate the PMP for each dam independently due to the areal limitation. USACE (2019) estimated the 72-hr PMP for many dams in the CRB using the traditional storm maximization approach. In their study, the PMP for each dam's drainage area was estimated considering that each dam is meteorologically and hydrologically independent (USACE, 2019).

A numerical weather model (NWM)-based PMP estimation approach has been developed to overcome the aforementioned limitations. The NWM-based approach estimates the PMP by numerically solving the nonlinear governing equations of the regional atmospheric processes. Hence, the NWM-based approach does not depend on the traditional assumptions, such as the linear relationship between precipitation depth and PW, and does not have a limitation on the spatial extent of the PMP estimation as long as the computational resources allow. Recently, Ohara et al. (2011) proposed a NWM-based PMP estimation approach which modifies the initial and boundary conditions (ICs, BCs) at the outer nesting domain of the NWM for maximizing precipitation. The approach of Ohara et al. (2011) consists of a combination of the relative humidity maximization (RHM) and the geospatial atmospheric BC shifting, following the general concepts of the traditional storm maximization approach. Hereafter, the geospatial atmospheric BC shifting will be referred to as "shifting". In the RHM method, the atmospheric moisture in the modeling domain is maximized by setting the relative humidity (RH) to 100% at ICs and BCs of the NWMs. The shifting method spatially shifts the atmospheric BCs of the NWMs so that target storms can be transposed to the specified watersheds. In Ishida et al. (2015a,b), the severe historical storms over three watersheds in Northern California were maximized using the shifting and RHM methods to obtain the PMP for a 72-h duration. Rastogi et al. (2017) estimated the PMP for 6 to 72 h storm durations using the RHM method under changing climate over the southeastern United States. Toride et al. (2019) developed a PMP estimation framework using the relative humidity perturbation (RHP) method, which proportionally increases RH at ICs and BCs of the modeling domain instead of setting RH at 100%, in order to maintain the original structure of RH (Yang and Smith, 2018). Toride et al. (2019) applied the RHP method only at the model boundaries where vertically integrated water vapor transport (IVT) values are higher than 250 kg m^{-1} s^{-1} (RHP-IVT method) to prevent unrealistic boundary conditions produced by applying the RHP method broadly across the boundary condition – to storm-free areas of the boundaries. The RHP-IVT method is detailed in Section 3 of this paper.

Although the NWM-based approach does not have a theoretical limitation on the spatial extent of the PMP estimation, few studies have focused on the PMP estimation for extremely large drainage areas (above 100,000 km^2; WMO, 2009) using the NWM-based approach. It is of great interest to apply the NWM-based approach to estimating the PMP for large drainage areas since it could be essential to evaluate the safety of hydraulic structures whose drainage areas are very large, such as that of Bonneville Dam.

Moreover, even though the NWM-based approach has been successfully applied to estimate the PMP with a single storm duration (mostly hourly to daily scale durations), little attention has been given to the PMP estimation for long durations, such as seasonal scale durations on the order of several months. The PMP estimation for long durations is crucial especially for snowmelt-driven regions, such as the CRB (U.S. Weather Bureau, 1945). In snowmelt-driven regions, extreme floods are often driven by both snow accumulation and snowmelt processes rather than by a single rainstorm event. It has been reported that extreme floods in the CRB are strongly dominated by winter snow accumulation and spring melt (Hamlet and Lettenmaier, 1999; Lee et al., 2009). These snow accumulation and snowmelt processes usually last on the order of several months, such as from the winter to early spring season. Therefore, the long-duration sequence of extreme precipitation or other atmospheric variables, such as temperature, is necessary for conducting the hydrologic precipitation-runoff analysis to estimate PMF in snowmelt-driven regions. This extreme precipitation sequence is also needed for long-duration water resource planning and management. The approaches mentioned above cannot be applied directly to the long-duration PMP estimation. This is because extreme precipitation for long durations, especially for large basins, is often composed of a sequence of successive short duration storm events from different synoptic systems, rather than from a single storm event (Liu et al., 2018; WMO, 2009). As a way of estimating the PMP for long durations, WMO (2009) suggests the "similar process substitution method". In this method, the storm processes with small rainfalls are temporally substituted with one or more storm processes with similar weather systems and large rainfalls to form a new sequence of ideal extraordinary storms. This method, however, requires sufficient hydrometeorological data, as well as theories and experience in mid- to long-term evolution of the regional weather systems to judge whether it is possible to reasonably link different storms together (WMO, 2009). Hence, the similar process substitution method is only applicable to a limited number of watersheds where sufficient observation data are available, and highly depends on the subjective judgment of hydrometeorologists.

Based on the above discussion, a new framework to estimate the PMP

for large basins and long durations during the winter and spring season, is required for the extreme flood risk assessment in snowmelt-driven regions. This study proposes a new framework to estimate the long-duration maximum precipitation (MP) during the winter season for large basins dominated by atmospheric rivers (ARs) using the NWM-based approach. We call this effort a "MP" which is defined as a part of PMP, due to the fact that, in such a long duration flooding regime, the ultimate PMP estimation requires the sequence of extreme precipitation during both the winter and spring season. This study, which is the first part of a two-part effort to develop the PMP estimation during the winter and spring season, focuses on the winter season MP estimation which addresses the AR-induced extreme precipitation and snowpack accumulation during the winter season. The second part of the ongoing effort, not discussed in this paper, will address the MP estimation during the spring season focusing on the spring rain on snow events and snowmelt process that often yields extreme floods in snow-dominated regions. As a demonstrative case, we estimate the MP for the 6-month winter period (October-March) for the drainage areas of Bonneville Dam and Libby Dam in the CRB. The estimated winter season MP in this paper can be used later to develop the PMP during the winter and spring (April-June) seasons. We estimate the MP for the 6-month winter period by maximizing all identified AR events belonging to the specified period in a target water year by optimizing the AR position and its atmospheric moisture. In this paper, the term "optimization'' is used to describe the combination of the AR position and its atmospheric moisture that maximizes the precipitation depth during the target historical AR event, as defined in Toride et al. (2019). Additionally, in this paper, "maximizing AR event" means maximizing the cumulative basin-average precipitation depth over the target basin during the target AR event period. Section 2 of this paper reviews the study area, numerical weather model, and data. Section 3 describes the framework for the long-duration MP estimation. Section 4 provides the simulation results. Section 5 summarizes and discusses these results.

2. Material and methods

2.1. Study area

The CRB is located in the Pacific Northwest, extending over seven U. S. states and southern British Columbia, Canada, which consists of 13 main tributary drainage areas (Fig. 1). The Columbia River (CR) is the largest river in the Pacific Northwest and fourth-largest river in North America, traveling over 2000 km (1,240 miles) and draining roughly 673,400 km^2 (260,000 sq mi) (Cohen et al., 2000; U.S. Department of the Interior, Bureau of Reclamation, 2016).

In the CRB, there are more than 250 reservoirs and around 150 hydroelectric projects providing 60–70% of the electrical needs in the Pacific Northwest region in the U.S., with 31 major federal dams including Bonneville Dam and Libby Dam (U.S. Department of the Interior, Bureau of Reclamation, 2016). The total drainage area above Bonneville Dam is about 621,600 km^2 (240,000 sq mi), and includes 11 watersheds: Upper Columbia, Kootenai, Pend Oreille, Middle Columbia, Spokane, Yakima, Lower Snake, Deschutes, Mainstem, Upper Snake, and Middle Snake watershed, shown in Fig. 1 (USACE, 2019). The total drainage area of Libby Dam is 23,270 km^2 (8,985 sq mi), shown as the gray shaded area in Fig. 1 (USACE, 2019). In this study, we focus on the drainage areas of Bonneville Dam and Libby Dam in the CRB to estimate the long-duration MP.

The CRB experienced significant floods in 1876, 1894, 1948, and 1996 (Stanford et al., 2005). The flood of June 1894 recorded the greatest flow discharge, reaching 33.6 ft (10 m) water level at Portland (Flores and Griffith, 2002; Willingham, 2014), while the flood stage for the CR, as measured near the Port of Vancouver, was 16.0 ft (4.9 m) (National Weather Service, 2019). The flood of June 1894 is regarded as one of the world's largest floods (O'Connor and Costa, 2004), which was caused by heavy snowpack accumulated during the winter of 1893–1894, followed by a dry, warm spring, resulting in massive

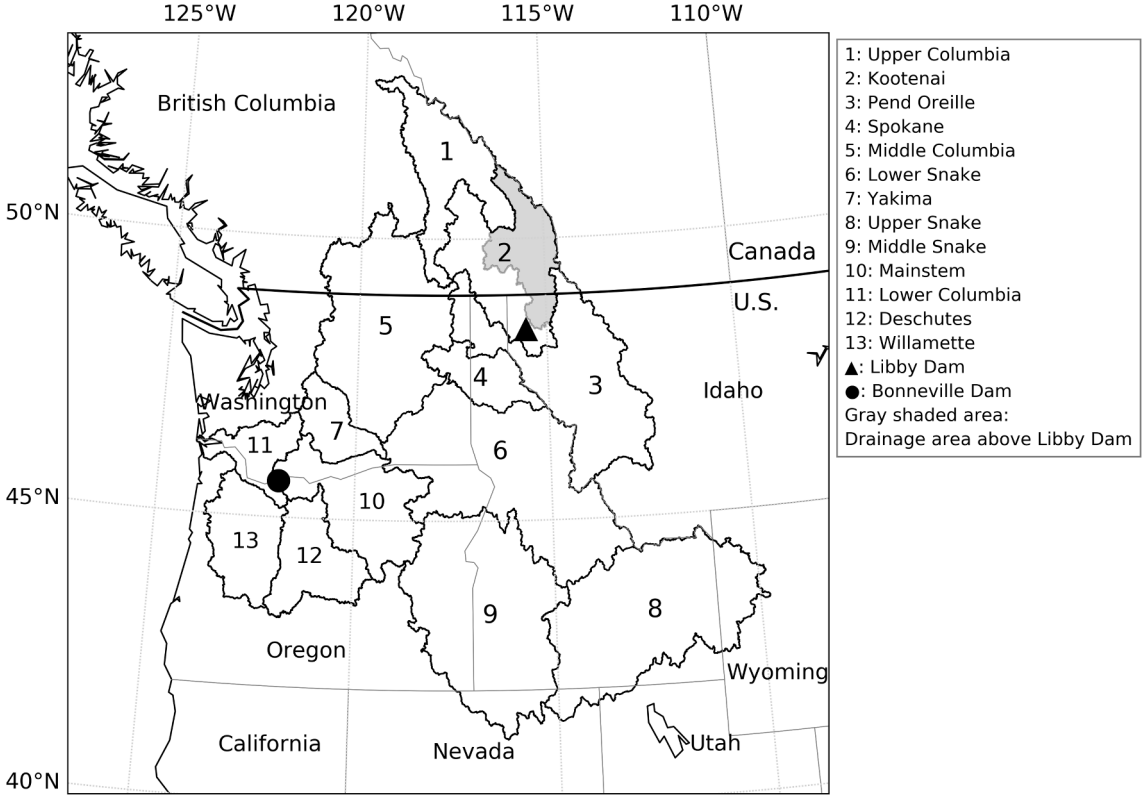

Fig. 1. Location map of the Columbia River Basin (CRB) and the drainage areas of Bonneville Dam and Libby Dam. Bonneville Dam's drainage area includes 11 watersheds: Upper Columbia, Kootenai, Pend Oreille, Middle Columbia, Spokane, Yakima, Lower Snake, Deschutes, Mainstem, Upper Snake, and Middle Snake watershed.

snowmelt (Nelson, 1949). The second-largest flow discharge in the CRB was recorded for the flood of May-June 1948, reaching 31.0 ft (9.4 m) water level at Portland (McGregor, 2003). Extreme rainfall on the snow which was accumulated in the winter and early spring and sharply increased the temperature in May and June produced this hazardous flood with the estimated damage of more than 100 million dollars (Rantz and Riggs, 1949).

Along the Pacific Northwest region where the CRB is located, ARs play a critical role in transporting massive amounts of water vapor from the eastern Pacific Ocean, contributing to the majority of wintertime extreme precipitation (Knippertz and Wernli, 2010; Neiman et al., 2008; Warner et al., 2012). ARs are defined as long and narrow corridors of strong IVT (Ralph et al., 2004; Zhu and Newell, 1998). Recent studies showed that the central CRB is largely affected by the AR-generated precipitation and floods (Barth et al., 2017; Rutz et al., 2014). Ralph and Dettinger (2012) showed that ARs fed more than 90% of the heaviest 3-day rain events in the U.S. West Coast. Neiman et al. (2011) reported that about 95% of the annual peak daily flow occurred with landfalling ARs in Western Washington. In this paper, IVT is calculated by the following equation (Chen, 1985; Newell et al., 1992; Neiman et al., 2008):

$$IVT = \frac{1}{g}\int_{1000}^{300} q\overline{U}dp \tag{1}$$

where g is the gravitational acceleration (m s^{-2}), q is the specific humidity (kg kg^{-1}), $\overline{U}$ is the horizontal wind speed (m s^{-1}), and p is the pressure (hPa). ARs are generally identified using the threshold of IVT > 250 kg m^{-1} s^{-1} over the Pacific Northwest region (Rutz et al., 2015, 2014).

2.2. Model and data

The Advanced Research version of Weather Research and Forecasting Model (WRF), version 3.9.1, was used for conducting numerical experiments to estimate the long-duration MP in this study. WRF is a fully compressible and non-hydrostatic model using a terrain-following hydrostatic-pressure vertical coordinate and an Arakawa C-grid staggering spatial discretization for atmospheric variables (Skamarock et al., 2008). The model configuration consists of two nested domains with horizontal grid resolutions of 36 km and 12 km. Fig. 2 shows the geographic coverage of the domains. Two-way nesting was employed, so that information from the inner domain was carried back to the outer domain. Both model domains have 40 sigma levels from the surface to 50 hPa. The outer domain covers the west coast of North America from Southern California to middle British Columbia while the inner domain covers the whole CRB.

For the initial conditions and boundary conditions in the WRF model, this study used the National Centers for Environmental Prediction's (NCEP) Climate Forecast System Reanalysis (CFSR; Saha et al., 2010) and the National Oceanic and Atmospheric Administration (NOAA) Twentieth Century Reanalysis version 2c (20CRv2c; Compo et al., 2011). This study also used the CFSR and 20CRv2c for calculating IVT used in the AR event identification process (detailed in Section 3.2). The CFSR is a global reanalysis product generated by a coupled ocean–atmosphere general circulation model by assimilating various observations (Saha et al., 2010). The CFSR is available from 1979 to present at 6-hour intervals with 0.5° horizontal resolution and 40 vertical levels. 20CRv2c is a global reanalysis product generated by assimilating only surface pressures and using monthly sea surface temperature and sea ice distributions as boundary conditions within an Ensemble Kalman Filter (Compo et al., 2011). The 20CRv2c is available from 1850 to 2014 at 6-hour intervals with 2.0° spatial resolution and 24 vertical levels. In this

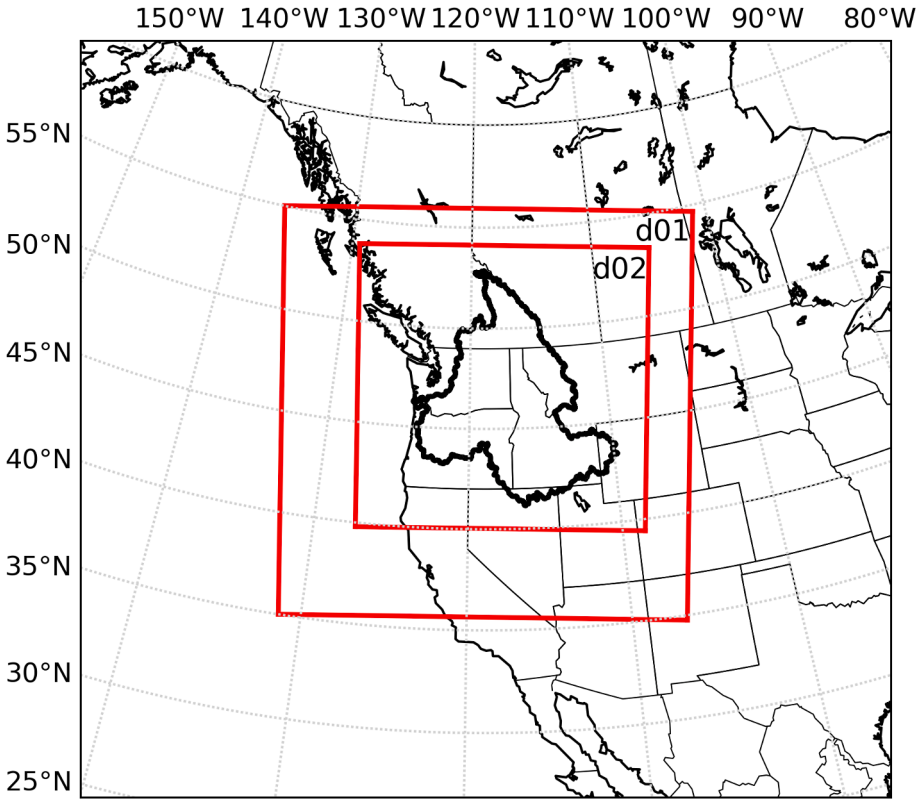

Fig. 2. Domain configuration for the WRF simulations. Domains 1 and 2 employ horizontal grid spacings of 36 km and 12 km, respectively.

study, the reanalysis product was selected depending on the target water year: CFSR for the 2017 water year and 20CRv2c for the 1974 water year. Selection of the target water years is detailed in Section 3.1.

The physical parameterization schemes used in the model domains include the Rapid radiative transfer model for general (RRTMG) short radiation scheme (Iacono et al., 2008), the RRTMG longwave radiation scheme (Iacono et al., 2008), the Stony-Brook University microphysics scheme (Lin and Colle, 2011), the Mellor-Yamada-Janjic planetary boundary layer scheme (Janjić, 1994), the Zhang-McFarlane cumulus convection scheme (Zhang and McFarlane, 1995), and the Noah land surface model (Ek et al., 2003). This parameterization configuration was selected following the CONUS physics suite which is available in the WRF version 3.9, except for the microphysics and cumulus convection schemes. This study investigated the performance and sensitivity of the parameterization schemes for simulating the basin-average precipitation and temperature in the CRB, resulting in the selection of the different microphysics and cumulus convection schemes from the CONUS physics suite. To evaluate the selected parameterization configuration, the simulated CRB basin average precipitation was compared to the gridded Parameter-Elevation Regressions on Independent Slopes Model (PRISM; Daly et al., 2008) dataset. The PRISM dataset provides the interpolated ground observed precipitation and temperature data over the U.S. with 4-km spatial resolution. The PRISM dataset has a daily product from 1979 to present and a monthly product from 1895 to present. Thus, the WRF simulation results were compared to the PRISM daily product for the 2017 water year and to the PRISM monthly product for the 1974 water year. Fig. S1 shows the comparison of the daily CRB-average precipitation depth from October 01, 2016 to March 31, 2017. From Fig. S1, the daily CRB-average precipitation simulated with the selected parameterization schemes shows good agreement with the PRISM dataset ($R^2 = 0.87$). Fig. S2 shows the comparison of the monthly CRB-average precipitation depth from October 01, 1973 to March 31, 1974. In Fig. S2, although the WRF simulation tends to overestimate the monthly CRB-average precipitation depth, it captures the temporal variation in the precipitation depth quite well ($R^2 = 0.94$).

3. Proposed framework for the long-duration MP estimation during a winter season

In this study, a new framework is proposed to estimate the long-duration MP during the winter season in AR dominant regions as follows:

Step 1: Select target water years based on the historical precipitation depth and average temperature over a specified basin;
Step 2: Identify historical AR events over a specified basin during the winter season in the target water years based on the AR category scale developed by Ralph et al. (2019);
Step 3: Maximize the cumulative precipitation depths over the target drainage areas within a specified basin during the identified AR events by simultaneously optimizing the AR position and atmospheric moisture;
Step 4: Substitute each historical AR event with the corresponding maximized AR event to form the sequence of maximized precipitation events (design precipitation sequence) during the winter season;
Step 5: Develop the long-duration MP estimation during the winter season over the target drainage areas by accumulating the design precipitation sequence formed in the above step 4.

The procedure at each step is detailed below.

3.1. Selection of target water years

In step 1, target water years for the MP estimation for the 6-month winter period (October-March) are selected based on their historical precipitation depth during the winter season over the CRB. This procedure is based upon the hypothesis that water years with heavy precipitation during the winter season have high potential to produce the long-duration MP. Table. 1 which was created using the PRISM dataset, shows the top 15 water years with respect to the accumulated CRB-average precipitation depths during the winter season for the period of 1928–2020 water years. Besides the precipitation depths, Table. 1 shows the ranking of the time-averaged CRB-average temperature during the spring season for the period of 1928–2020 water years. In this study, the 1974 and 2017 water years were selected to demonstrate the MP estimation for the 6-month winter season over the CRB. The 1974 water year was selected since it shows the greatest CRB-average precipitation depth during the winter season for the period of 1928–2020 water years (Table. 1). The 2017 water year was selected because it also shows significant CRB-average precipitation depth during the winter season (4th largest) with the highest spring season temperature among the 15 water years shown in Table. 1. It should be noted that water years with heavy precipitation during the winter season and high temperature during the spring season, could be the basis of a PMP scenario during the winter and spring season in the CRB where extreme floods are typically caused by the spring snowmelt process (Lee et al, 2009). Therefore, the 2017 water year was selected considering the high spring season temperature although the MP estimation during the spring season is not covered in this study.

3.2. Identification of historical Atmospheric River events

In step 2, the historical AR events during the winter season in the selected water years were identified based on the IVT thresholds used in the recently developed AR category scale (Ralph et al., 2019). This category scale classifies AR events into five categories: Primarily beneficial (category 1), Mostly beneficial but also hazardous (category 2), Balance of beneficial and hazardous (category 3), Mostly hazardous but also beneficial (category 4), and Primarily hazardous (category 5), using the maximum IVT magnitude and the duration of the AR event at a given point (Ralph et al., 2019). The "AR event" is defined in Ralph et al. (2019) by the period during which IVT at a given point location continuously satisfies the threshold: IVT $\geq$ 250 kg m^{-1} s^{-1}. In this study, the AR event period is defined by the duration that maximum IVT over the CRB continuously satisfies the same threshold: IVT $\geq$ 250 kg m^{-1} s^{-1}. The maximum IVT magnitude over the CRB is also considered to

Table 1
Top 15 winter season accumulated basin-average precipitation depths and spring season average basin-average temperature in the corresponding water years over the Columbia River Basin for the 1928–2020 water years. The winter season is from October to March; the spring season is from April to June. This table was created based on the PRISM dataset.

Ranking (precipitation)	Water year	Cumulative CRB-average precipitation depth during the winter season [mm]	Ranking (temperature)	Average CRB-average temperature during the spring season [°C]
1	1974	733.6	53	11.8
2	1997	688.7	68	11.4
3	1956	665.1	29	12.4
4	2017	657.3	21	12.7
5	1996	621.6	58	11.6
6	1972	615.0	60	11.5
7	1971	607.3	74	11.3
8	1982	605.3	84	10.8
9	1951	603.0	50	11.9
10	1999	592.9	90	10.5
11	1943	585.1	67	11.4
12	1938	581.9	27	12.4
13	1950	580.7	82	10.9
14	1976	573.9	73	11.3
15	1965	573.6	65	11.5

identify the AR events belonging to the categories 2–5, which could be hazardous. The following are the IVT thresholds that were applied to identify the AR events belonging to the categories 2–5 in Ralph et al. (2019).

- AR event duration $<$ 24 h & Maximum IVT over the CRB $\geq$ 750 kg m^{-1} s^{-1}
- AR event duration $\geq$ 24 h and $<$ 48 h & Maximum IVT over the CRB $\geq$ 500 kg m^{-1} s^{-1}
- AR event duration $\geq$ 48 h & Maximum IVT over the CRB $\geq$ 250 kg m^{-1} s^{-1}

The IVT over the region including North America and the Pacific Ocean was calculated using the reanalysis datasets: CFSR for the 2017 water year and 20CRv2c for the 1974 water year. The identified AR events during the winter season in the 2017 and 1974 water years are listed in Table 2 and Table 3, respectively. Twenty-four AR events were identified during the winter season in the 2017 water year and 16 AR events were identified during the winter season in the 1974 water year. The IVT contours over the CRB during the AR event 12-b in the 1974 water year: 1200 UTC Jan 12, 1974–1200 UTC Jan 17, 1974 are shown in Fig. 3. The AR event 12-b showed the greatest maximum IVT over the CRB among all the identified events (1042.5 kg m^{-1} s^{-1}). From the figure, one can see how the AR event enters and passes through the CRB with time.

Table 2
The identified atmospheric river events over the Columbia River Basin during the winter season in the 2017 water year. This table was created based on the CFSR reanalysis dataset.

AR event number	Start	End	Duration [hr]	Maximum IVT over the CRB [kg m^{-1} s^{-1}]
1-a	2016-10-07 00:00	2016-10-11 18:00	114	722.0
2-a	2016-10-13 00:00	2016-10-18 00:00	120	906.3
3-a	2016-10-20 00:00	2016-10-22 06:00	54	673.0
4-a	2016-10-24 00:00	2016-11-01 06:00	198	791.2
5-a	2016-11-02 00:00	2016-11-03 12:00	36	578.1
6-a	2016-11-05 00:00	2016-11-06 18:00	42	700.0
7-a	2016-11-07 00:00	2016-11-09 18:00	66	468.7
8-a	2016-11-11 00:00	2016-11-13 06:00	54	649.2
9-a	2016-11-13 12:00	2016-11-16 12:00	72	699.6
10-a	2016-11-24 06:00	2016-11-27 00:00	66	538.6
11-a	2016-12-08 18:00	2016-12-11 00:00	54	451.8
12-a	2016-12-14 12:00	2016-12-16 18:00	54	527.4
13-a	2016-12-19 06:00	2016-12-21 00:00	42	661.2
14-a	2017-01-07 18:00	2017-01-09 18:00	48	565.4
15-a	2017-01-10 12:00	2017-01-11 12:00	24	545.5
16-a	2017-01-17 00:00	2017-01-19 12:00	60	804.4
17-a	2017-02-03 12:00	2017-02-08 12:00	120	633.4
18-a	2017-02-08 18:00	2017-02-11 00:00	54	813.7
19-a	2017-02-15 00:00	2017-02-17 06:00	54	788.0
20-a	2017-02-20 12:00	2017-02-22 00:00	36	528.6
21-a	2017-03-07 12:00	2017-03-11 00:00	84	601.9
22-a	2017-03-11 18:00	2017-03-16 18:00	120	751.8
23-a	2017-03-17 12:00	2017-03-20 06:00	66	769.2
24-a	2017-03-28 12:00	2017-03-31 00:00	60	629.9

Table 3
The identified atmospheric river events over the Columbia River Basin during the winter season in the 1974 water year. This table was created based on the 20CRv2c reanalysis dataset.

AR event number	Start	End	Duration [hr]	Maximum IVT over the CRB [kg m^{-1} s^{-1}]
1-b	1973-10-06 12:00	1973-10-08 00:00	36	502.6
2-b	1973-10-12 06:00	1973-10-14 12:00	54	554.1
3-b	1973-10-17 18:00	1973-10-22 00:00	102	462.0
4-b	1973-10-27 06:00	1973-10-29 00:00	42	508.1
5-b	1973-10-30 00:00	1973-11-01 12:00	60	517.5
6-b	1973-11-05 12:00	1973-11-13 00:00	180	644.7
7-b	1973-11-14 18:00	1973-11-17 00:00	54	437.0
8-b	1973-11-27 06:00	1973-11-29 18:00	60	510.4
9-b	1973-12-06 06:00	1973-12-08 00:00	42	513.3
10-b	1973-12-15 06:00	1973-12-17 18:00	60	607.6
11-b	1973-12-20 00:00	1973-12-21 18:00	42	583.4
12-b	1974-01-12 12:00	1974-01-17 12:00	120	1042.5
13-b	1974-01-18 12:00	1974-01-19 12:00	24	663.3
14-b	1974-02-18 06:00	1974-02-19 12:00	30	516.9
15-b	1974-02-28 00:00	1974-03-02 12:00	60	465.2
16-b	1974-03-14 18:00	1974-03-17 00:00	54	330.2

3.3. Maximization of the identified Atmospheric River events

In step 3, the cumulative basin-average precipitation depths during the identified AR events are maximized by simultaneously optimizing the AR position and atmospheric moisture. The shifting and RHP-IVT operations were simultaneously conducted for the optimization. The RHP-IVT method proportionally increases the RH at the modeling boundary where IVT value exceeds 250 kg m^{-1} s^{-1}, as follows:

$$RH = \begin{cases} min(\beta RH_0,\ 97),\ if\ RH_0 < 97\% \\ RH_0,\ if\ RH_0 \geq 97\% \end{cases} \quad (2)$$

where RH_0 is the original relative humidity (%) and β is a multiplication factor to determine the increment of RH. In Eq. (2), the threshold is set to 97% in order to avoid immediate saturation at the modeling domain (Zhao et al., 1997). Hereafter, the RHP-IVT method with $\beta = 1.1$ is referred to as RHP110-IVT, RHP120-IVT with $\beta = 1.2$, and so on (Toride et al. 2019). The procedure for maximizing the identified AR events using the combination of the shifting and RHP-IVT operations is detailed as follows:

Step 3-1: Apply the latitudinal shifting up to 5° in north and south directions at 0.5° intervals with RHP110-IVT (Shift + RHP110-IVT) to the AR events. In this study, the atmospheric boundary conditions were shifted with respect to latitude only. The shifting with respect to

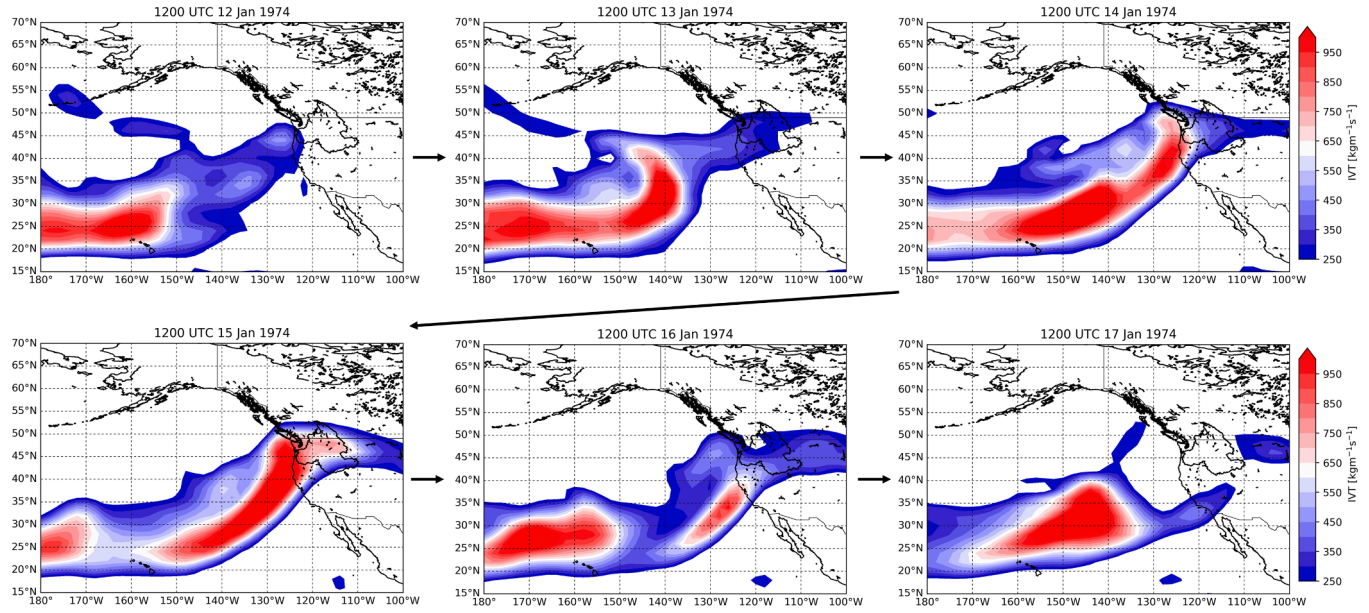

Fig. 3. Integrated water vapor transport (IVT; kg m^{-1} s^{-1}) contours during the atmospheric river event 12-b in the 1974 water year: 1200 UTC Jan 12, 1974–1200 UTC Jan 17, 1974. The visualized fields are based on the 20CRv2c dataset.

longitude could render unrealistic atmospheric conditions over the CRB due to the land-sea contrast in the surface layer since the CRB is located along the Pacific Northwest coast. The latitudinal range of the shifting is limited to 5° in north and south directions so that the Coriolis parameter component of the absolute vorticity of the system would not change by more than 10 percent (Hansen et al. 1994). In this study, the RHP110-IVT was first applied in order to investigate the sensitivity of the basin-average precipitation increase to the increase in atmospheric moisture at each shifting amount.

Step 3-2: Apply the latitudinal shifting with RHP-IVT with β ranging from 1.2 to 1.5 at 0.1 intervals (RHP120-IVT, RHP130-IVT, RHP140-IVT, and RHP150-IVT) to the AR events. In this step, the shifting amount was determined according to the sensitivity of the basin-average precipitation increase to RH increase, investigated in step 3-1. The increments of β were limited up to 1.5 since a large increase in atmospheric moisture may change storm evolution and structural properties (Ohara et al., 2017; Yang and Smith, 2018). It was also shown that excessive RH increase does not necessarily lead to a rise in precipitation depths (Ohara et al., 2017; Yang and Smith, 2018). In Toride et al. (2019), the 72-h PMP in the Willamette watershed was obtained by the combination of shifting and RHP130-IVT although they investigated the RHP-IVT with β up to 1.7 (RHP170-IVT).

Step 3-3: Apply the latitudinal shifting at 0.1° intervals with the optimal RHP-IVT found in step 3-2 to the AR events. The latitudinal shifting amount was set up to 0.5° north and south of the north-south location at which the AR event cumulative basin-average precipitation depth became greatest in step 3-2. In other words, this procedure aims to find an actual maximum basin-average precipitation depth by a local search with finer intervals around the optimal north-south location with the optimal RHP-IVT found in step 3-2.

In this study, first, step 3-1 was conducted for all identified AR events over the CRB during the winter season in each target water year. Then, step 3-2 and step 3-3 were performed for the drainage areas of Bonneville Dam and Libby Dam, respectively. It is noted that each AR event simulation was initialized using the WRF restart files of the control simulation so that each AR event could be maximized based on the historical conditions.

3.4. Development of long-duration MP estimation during the winter season

In step 4, each historical AR event was substituted with the corresponding maximized AR event in order to form a sequence of maximized precipitation depths during the winter season. In this paper, the resulting sequence of maximized precipitation depths during the winter season is called “design precipitation sequence”. This AR event substitution is based on the concept of the similar process substitution method in which historical storms with small rainfalls are substituted with one or more historical storms with large rainfalls (WMO, 2009). The design precipitation sequence was formed for the drainage areas of Bonneville Dam and Libby Dam, respectively. In step 5, the 6-month winter season accumulated basin average precipitation depths were computed using the design precipitation sequence over the drainage areas of Bonneville Dam and Libby Dam, respectively. Finally, the maximum 6-month winter season accumulated precipitation depths were obtained as the long-duration MP during the winter season for Bonneville Dam and Libby Dam.

4. Results

4.1. Maximization of the historical Atmospheric River events

We first examine how each AR event is maximized through simultaneously optimizing the AR position and its atmospheric water vapor since the long-duration MP is obtained as a result of maximization of each AR event. Figs. 4 and 5 show the cumulative basin-average precipitation depths during each AR event, obtained by the control simulation, Shift + RHP110-IVT experiment, and the simulation with the optimal combination of the AR position and RH. The optimal combinations of the AR position and RH are shown with the AR event names in the figures (e.g., 5.0° S (N) + RHP150-IVT represents the combination of 5.0° south (north) shifting and RHP150-IVT). The figures also show the increasing rates in the basin-average precipitation depths from the control simulation’s results to the results of the simulations with the optimal combinations.

As shown in the figures, the AR events with relatively high potential to increase the basin-average precipitation depths can be identified. It is found that the optimal combination for each AR event depends on the

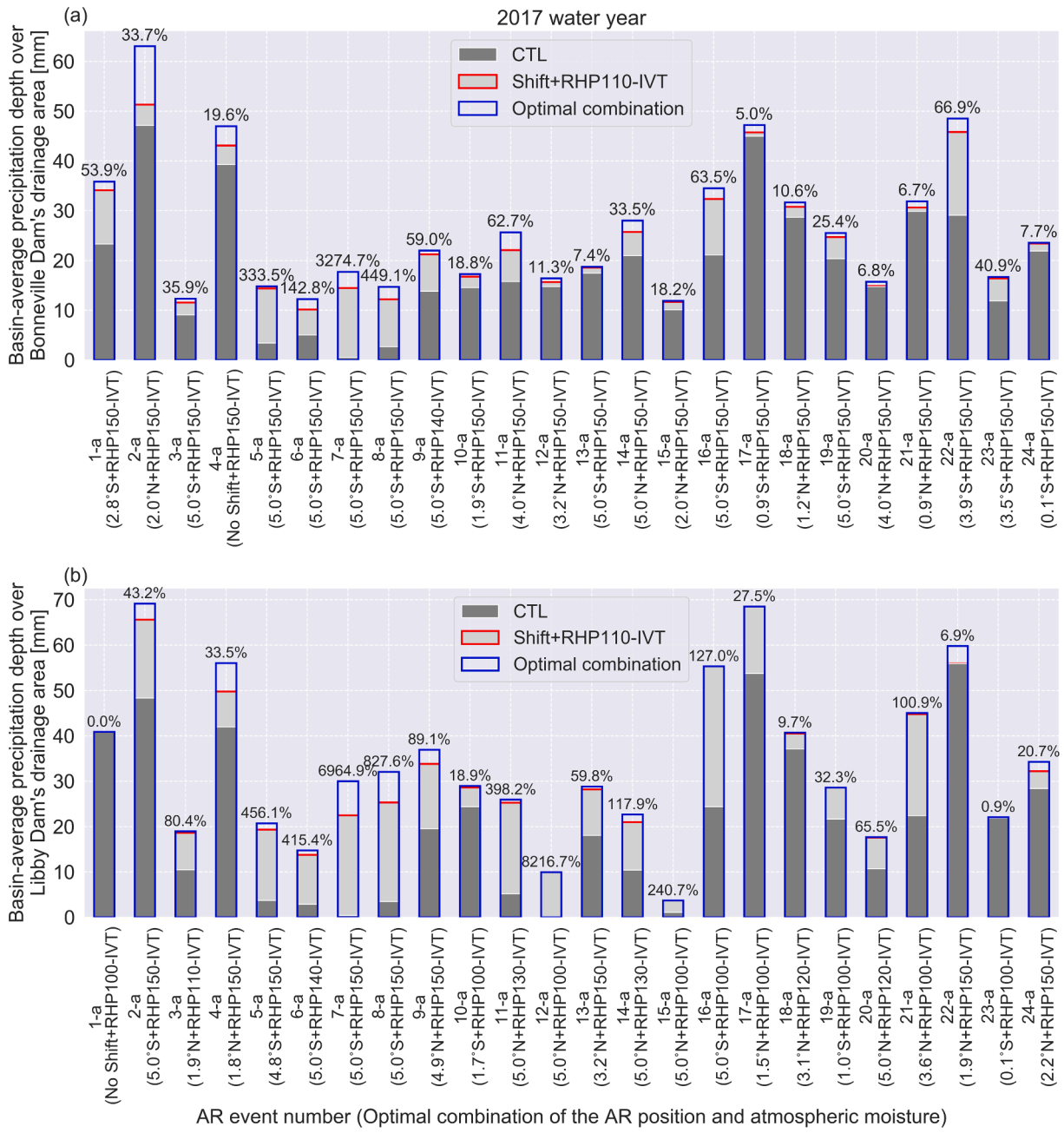

Fig. 4. The cumulative basin-average precipitation depths over the drainage areas of Bonneville Dam (a) and Libby Dam (b) during each atmospheric river (AR) event in the 2017 water year, obtained by the control simulation (CTL), Shift + RHP110-IVT experiment (Shift + RHP110-IVT), and the simulation with the optimal combination of the AR position and atmospheric moisture for each event (Optimal combination). The optimal combinations of the AR position and atmospheric moisture are shown with the AR event names. It shows the increasing rates in the cumulative basin-average precipitation depths during the AR events from the control simulation's results to the results of the simulations with the optimal combinations.

geographical characteristics of the target basin. As can be seen from Figs. 4 and 5, 15 AR events (62.5%) in the 2017 water year, and 10 AR events (62.5%) in the 1974 water year are maximized by south shifting for Bonneville Dam's drainage area. Meanwhile, 14 events (58.3%) in the 2017 water year and 11 events (68.8%) in the 1974 water year are maximized by north shifting for Libby Dam's drainage area. Moreover, 23 AR events (95.8%) in the 2017 water year and 14 AR events (87.5%) in the 1974 water year are maximized by RHP150-IVT for Bonneville Dam's drainage area; yet 10 AR events (41.7%) in the 2017 water year and 7 AR events (31.3%) in the 1974 water year are maximized without increasing RH or by RHP110-IVT for Libby Dam's drainage area. The relationship between the optimal combination and target basin can be more clearly found when focusing on specific events. For instance, the event 22-a in the 2017 water year is maximized by 3.9° south shifting and RHP150-IVT for Bonneville Dam's drainage area, but by 1.9° north shifting and RHP150-IVT for Libby Dam's drainage area (Fig. 4). Fig. 5 shows that the AR event 12-b in the 1974 water year is maximized by 5.0° south shifting and RHP150-IVT for Bonneville Dam's drainage area, yet by 4.9° south shifting and RHP100-IVT for Libby Dam's drainage area. To clarify how the optimal combination for each AR event is determined based on the geographical characteristics of the target basin or the event's properties, we investigate the atmospheric fields of the maximized AR events by comparing them with the control simulation's results.

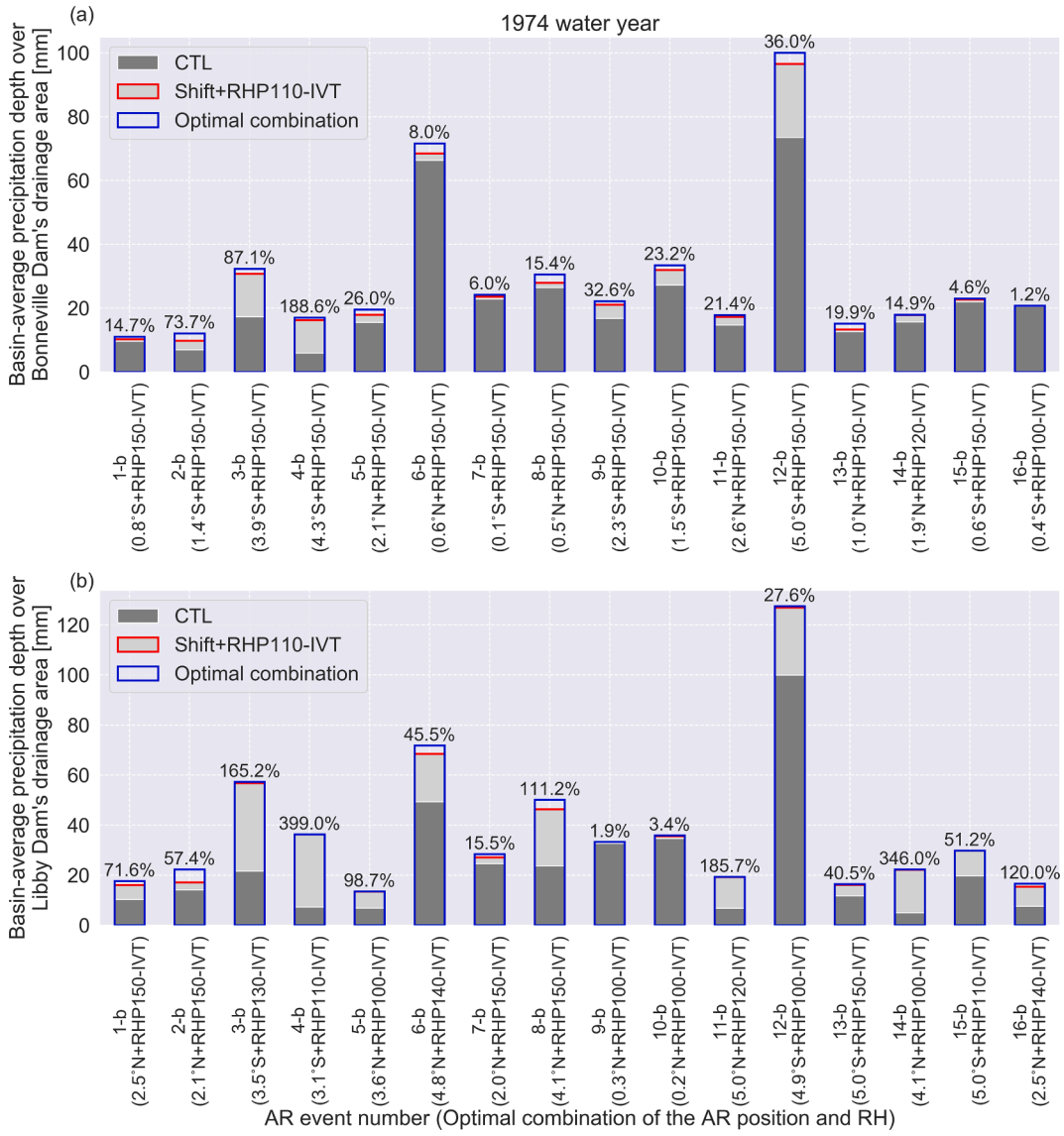

Fig. 5. The cumulative basin-average precipitation depths over the drainage areas of Bonneville Dam (a) and Libby Dam (b) during each atmospheric river (AR) event in the 1974 water year, obtained by the control simulation (CTL), Shift + RHP110-IVT experiment (Shift + RHP110-IVT), and the simulation with the optimal combination of the AR position and atmospheric moisture for each event (Optimal combination). The optimal combinations of the AR position and atmospheric moisture are shown with the AR event names. It shows the increasing rates in the cumulative basin-average precipitation depths during the AR events from the control simulation's results to the results of the simulations with the optimal combinations.

Fig. 6 shows the time-averaged IVT fields and spatial distributions of the accumulated precipitation depths obtained by the control simulation (Fig. 6a and d) and the simulation with the optimal combination for the drainage areas of Bonneville Dam (Fig. 6b and e) and Libby Dam (Fig. 6c and f) during the AR event 22-a in the 2017 water year. As can be seen from Fig. 6a, this AR event initially hits the region around Oregon to Washington state and extends to the central CRB in the control simulation. Fig. 6d shows that the region with high precipitation depths, such as the western CRB, corresponds to the strong IVT area. In the case of the optimization for Bonneville Dam's drainage area: 3.9° south shifting and RHP150-IVT (Fig. 6b and e), the region with strong IVT is transposed to further south and becomes wider compared to the control simulation's result. The region where IVT $\geq$ 250 kg m^{-1} s^{-1} extends to the southern CRB as the AR system is transposed to the south. Fig. 6e shows that the optimization for Bonneville Dam's drainage area increases the precipitation depths, especially in the southern part of the domain. Meanwhile, this AR event is maximized by 1.9° north shifting and RHP150-IVT for Libby Dam's drainage area (Fig. 6c and f). In this case, the intense IVT region is located slightly more north than the control simulation's result, corresponding to the modest shifting amount (Fig. 6c). Fig. 6c shows that the optimization increases IVT intensity overall without changing the pattern of the IVT field much. The region where IVT $\geq$ 250 kg m^{-1} s^{-1} covers more northern and eastern parts of the CRB where Libby Dam's drainage area is located. Accordingly, it increases the precipitation depths mainly in the northern part of the CRB, leading to greater precipitation depths over Libby Dam's drainage area (Fig. 6f). Fig. 6 visualizes how the shifting amount and direction are determined to maximize the contribution of the AR event to the basin-average precipitation over the target basin in the proposed method. Since the major part of Bonneville Dam's drainage area belongs to the southern CRB while Libby Dam's drainage area is located at the north-east of the CRB, the shifting amount and direction are determined based on each event's characteristics.

Similarly, Fig. 7 shows the time-averaged IVT fields and the spatial distributions of the accumulated precipitation depths during the AR event 12-b in the 1974 water year. As can be seen from Fig. 7a, this AR

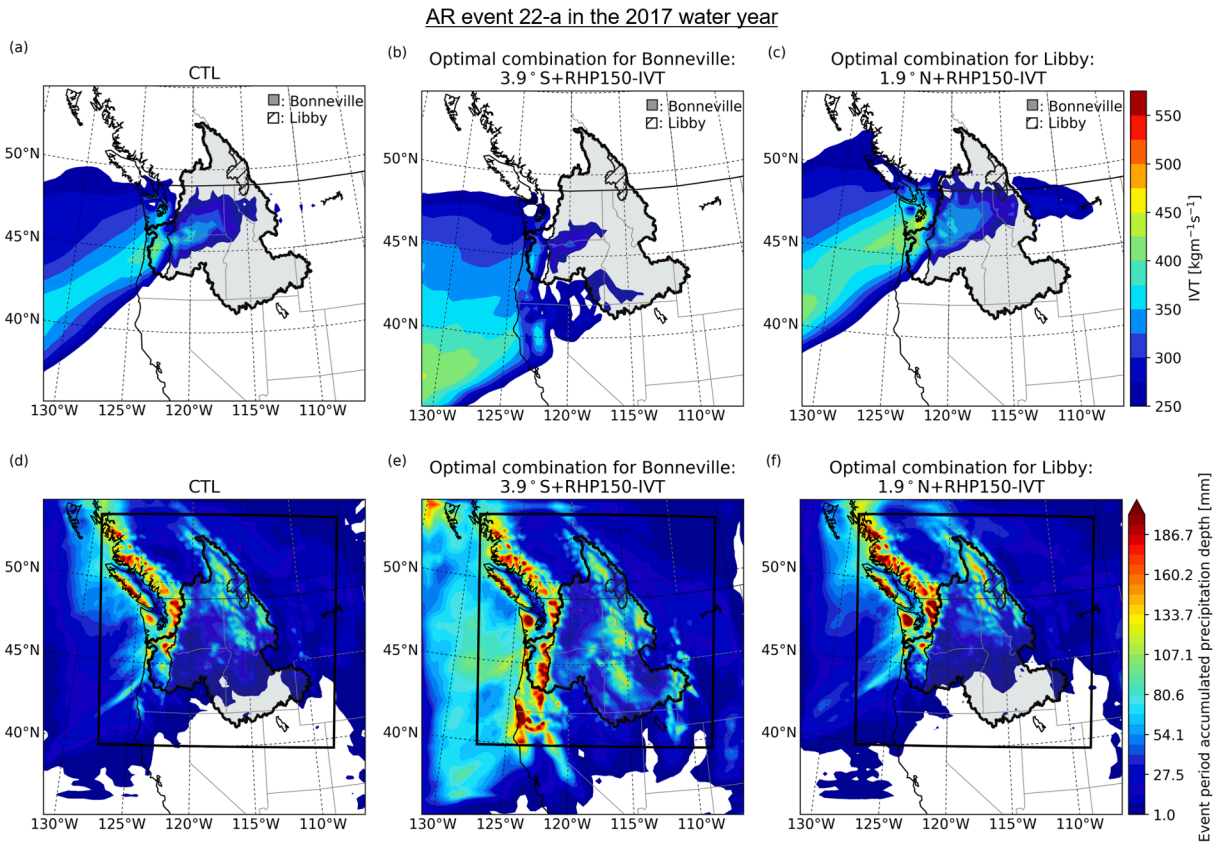

Fig. 6. The spatial distribution of the time-averaged Integrated water vapor transport (IVT; kg m^{-1} s^{-1}) (a-c) and accumulated precipitation depths (d-f) during the atmospheric river event 22-a in the 2017 water year (1800 UTC 11 Mar to 1800 UTC 16 Mar 2017): (a), (d) the control (CTL); (b), (e) the maximum case obtained by the simulation with the optimal combination for Bonneville Dam's drainage area (3.9° south latitudinal shifting + RHP150-IVT); (c), (f) the maximum case obtained by the simulation with the optimal combination for Libby Dam's drainage area (1.9° north latitudinal shifting + RHP150-IVT). "Bonneville" and "Libby" represent the drainage areas of Bonneville Dam and Libby Dam, respectively.

event hits the wide region ranging from Northern California to Washington state and covers a large portion of the CRB in the control simulation. The maximum IVT magnitude over the CRB during this event period is 1042.5 kg m^{-1} s^{-1} (Table. 3). In Fig. 7d, the high precipitation depths are distributed mainly in the coastal area and the eastern CRB. As the AR event is optimized by 5.0° south shifting and RHP150-IVT for Bonneville Dam's drainage area (Fig. 7b), the strong IVT region is transposed to the south, and the magnitude of IVT is intensified overall. In this case, almost the entire southern to central CRB is covered by the region with IVT $\geq$ 250 kg m^{-1} s^{-1}. Fig. 7e shows the significant increase in the precipitation depths within the modeling domain, especially at the eastern CRB as well as at the southern coastal area. The AR event optimized for Libby Dam's drainage area by 4.9° south shifting and RHP100-IVT, also shows a similar geospatial position transposed to the south (Fig. 7c). The IVT intensity overall becomes lower than the IVT intensity of the optimized case for Bonneville Dam's drainage area since atmospheric moisture is not increased. Accordingly, it shows lower precipitation depths, specifically in the south-west of the domain, compared to the optimized case for Bonneville Dam's drainage area (Fig. 7e and f). Interestingly, however, the precipitation depths over Libby Dam's drainage area become slightly greater, especially at the central part of Libby Dam's drainage area, than the optimized case for Bonneville Dam's drainage area (Fig. 7f). This phenomenon will be discussed in detail in Section 5.1.

Fig. 8 shows the changes in the cumulative basin-average precipitation depths through shifting and perturbing RH during the event 22-a (Fig. 8a and b) and event 12-b (Fig. 8c and d). Fig. 8a shows that the basin-average precipitation depth over Bonneville Dam's drainage area increases as the atmospheric BC is shifted toward the south, and peaks when it is shifted 3.9° south. The basin-average precipitation depth over Bonneville Dam's drainage area also monotonically increases with atmospheric moisture (Fig. 8a). Similarly, the basin-average precipitation depth over Libby Dam's drainage area peaks when the atmospheric BC is shifted 1.9° north (Fig. 8b). Importantly, Fig. 8b shows that the AR event maximization by modifying the AR position and RH is a non-linear process. Although the basin-average precipitation depth shows a monotonic increasing trend with RH when the atmospheric BC is shifted around 1.5°-2.5° north, it gradually diverges from this trend as the atmospheric BC is shifted toward the south of the optimal shifting location (Fig. 8b). This nonlinearity emphasizes the importance of the simultaneous optimization of the AR position and atmospheric moisture. Also, in the case of the AR event 12-b, although the basin-average precipitation over Libby Dam's drainage area increases with RH when the atmospheric BC is shifted 1.5°-2.0° south, the increment of the precipitation depth gradually decreases and turns to a decreasing trend as the atmospheric BC is shifted farther south. This non-linear change in the basin-average precipitation depth with shifting and RH perturbation, shown in Fig. 8d, will be discussed in Section 5.1.

We also analyzed the change in PW versus the change in precipitation depths due to the precipitation maximization. Fig. S3 and S4 show the relationships between the change in PW and the change in precipitation depths based on the maximization of the identified AR events in the 1974 and 2017 water years (Table. 2 and Table. 3) for Bonneville Dam's drainage area and Libby Dam's drainage area, respectively. As we can see from Fig. S3 and S4, the relationship assumed in the traditional storm maximization approach, which is the change in PW is consistent with the change in precipitation depth, is not present in our simulations. Although investigating this relationship further is beyond the scope of

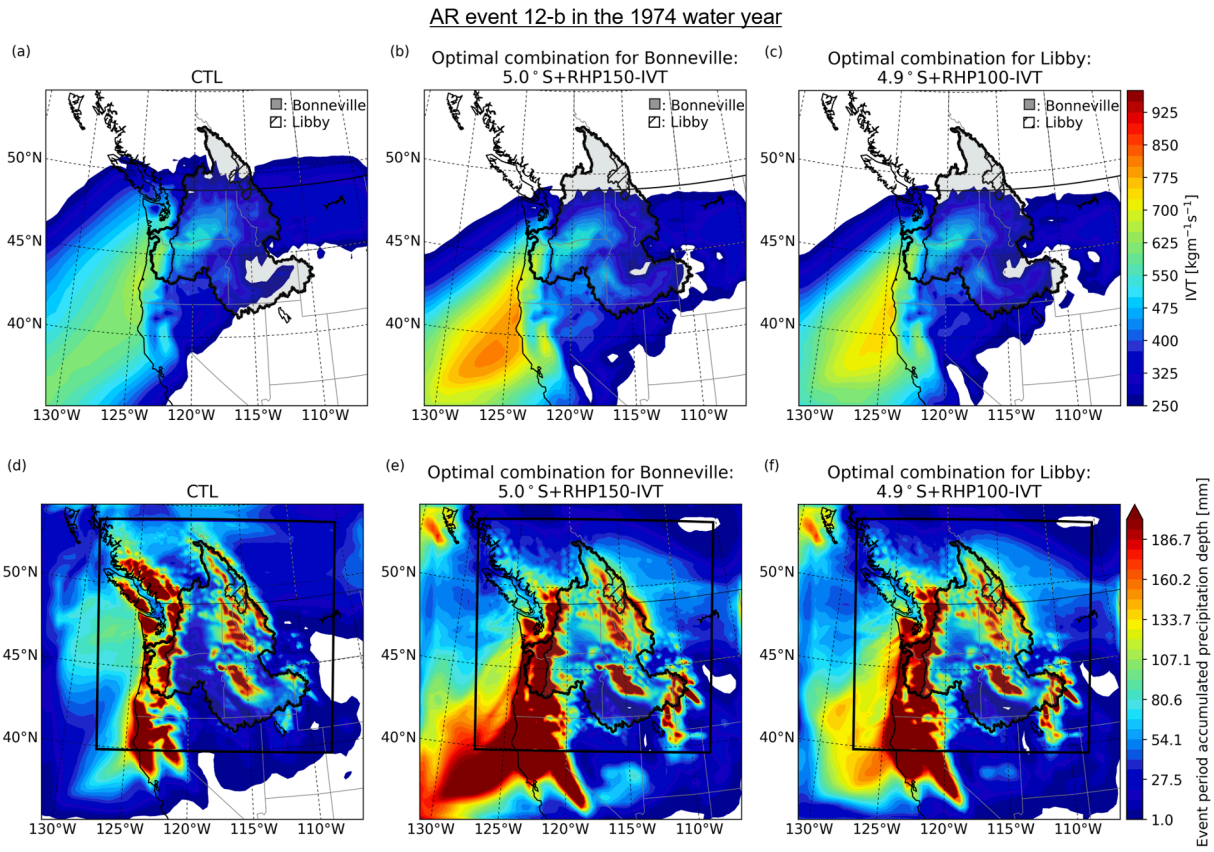

Fig. 7. The spatial distribution of the time-averaged Integrated water vapor transport (IVT; kg m^{-1} s^{-1}) (a–c) and accumulated precipitation depths (d-f) during the atmospheric river event 12-b in the 1974 water year (1200 UTC 12 Jan to 1200 UTC 17 Jan 1974): (a), (d) the control (CTL); (b), (e) the maximum case obtained by the simulation with the optimal combination for Bonneville Dam's drainage area (5.0° south latitudinal shifting + RHP150-IVT); (c), (f) the maximum case obtained by the simulation with the optimal combination for Libby Dam's drainage area (4.9° south latitudinal shifting + RHP100-IVT). "Bonneville" and "Libby" represent the drainage areas of Bonneville Dam and Libby Dam, respectively.

this paper, this finding could support the validity of the NWM-based approach which maximizes precipitation by accounting for non-linear atmospheric processes.

4.2. *Development of the MP estimation for the 6-month winter period*

The design basin-average precipitation sequence was formed by substituting each historical AR event with its corresponding maximized AR event. Fig. 9 shows the design basin-average precipitation sequence over Bonneville Dam's drainage area for the 6-month winter period. Similarly, Fig. 10 shows the design basin-average precipitation sequence over Libby Dam's drainage area. As can be seen from these figures, the maximized AR events result in significant changes in the basin-average precipitation depths during the corresponding AR event period. These figures show that the maximization process increases the precipitation peaks further, such as the strong peaks in the middle of January in the 1974 water year. When comparing the results for Bonneville Dam's drainage area (Fig. 9) with those for Libby Dam's drainage area (Fig. 10), the magnitude of the basin-average precipitation change by the optimization is generally higher in the Libby case than the Bonneville case. The change in basin-average precipitation should be greater in a smaller basin than the change in a larger basin for a given amount of precipitation change in a basin due to the smoothing effect of the spatial averaging which increases with basin size. Since Libby Dam's drainage area is much smaller than that of Bonneville Dam (Fig. 1), the basin-average precipitation over Libby Dam's drainage area is considered to be more sensitive to the to the optimization-induced precipitation change in a basin.

Fig. 11 shows the cumulative curve of the design basin-average precipitation together with the control simulation's results. The 6-month winter period accumulated basin-average precipitation depth over Bonneville Dam's drainage area increases 172.7 mm (23.3%) in the 2017 water year and 95.1 mm (11.0%) in the 1974 water year from the control simulation's results. Over Libby Dam's drainage area, it increases 304.9 mm (38.3%) in the 2017 water year and 223.0 mm (25.5%) in the 1974 water year from the control simulation's results. The amount of increase in the accumulated precipitation depth becomes larger over Libby Dam's drainage area than Bonneville Dam's drainage area since the magnitude of the precipitation change is found to be larger over Libby Dam's drainage area, as discussed above (Figs. 9 and 10). From Fig. 11, the maximum cumulative basin-average precipitation depth, namely long-duration MP, for the 6-month winter season is estimated to be 961.0 mm over Bonneville Dam's drainage area and 1101.7 mm over Libby Dam's drainage area.

The sensitivity of the increase in the cumulative basin-average precipitation depth to the AR transposition and RH perturbation was also investigated. Fig. 12 shows the 6-month winter period accumulated precipitation depths when the AR events are transposed to the optimal location for each atmospheric moisture condition. In Fig. 12, "Design" represents the 6-month winter period accumulation of the design precipitation sequence. As can be seen from Fig. 12, the latitudinal shifting accounts for the significant part of the increase in the basin-average precipitation depth: 63.6% of the total increase in the 2017 water year and 63.2% in the 1974 water year over Bonneville Dam's drainage area; 80.5% in the 2017 water year and 82.4% in the 1974 water year over Libby Dam's drainage area. Since ARs are narrow and long bands of strong IVT (Ralph et al., 2004; Zhu and Newell, 1998), the latitudinal transposition of ARs to the optimal locations significantly contributes to

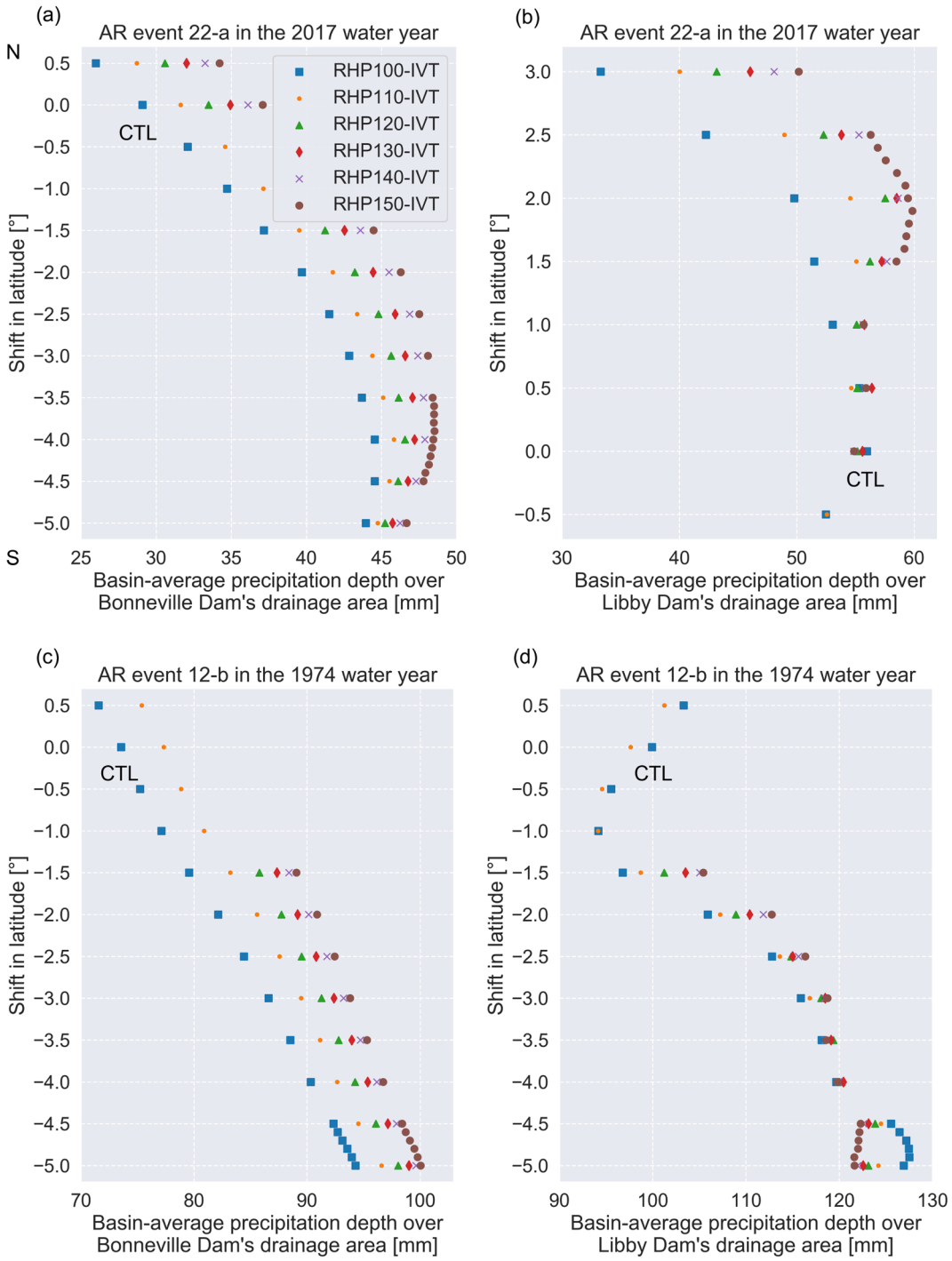

Fig. 8. The maximization process of the cumulative basin-average precipitation depths through latitudinal shifting and RH perturbations along atmospheric rivers (AR) over (a) Bonneville Dam's drainage area during the AR event 22-a in the 2017 water year; (b) Libby Dam's drainage area during the AR event 22-a in the 2017 water year; (c) Bonneville Dam's drainage area during the AR event 12-b in the 1974 water year; and (d) Libby Dam's drainage area during the AR event 12-b in the 1974 water year.

the increases in the basin-average precipitation depths. The atmospheric moisture increase plays a relatively larger role in increasing precipitation depth over Bonneville Dam's drainage area than Libby Dam's drainage area. The relationship between atmospheric moisture and precipitation depth, taking into account the differences in geographical characteristics of the target basins, will be discussed in detail in Section 5.1.

Fig. 13 shows the spatial distribution of the 6-month winter period accumulated precipitation depths over the modeling domain. In Fig. 13, "Design precipitation" shows the spatial distribution of the 6-month winter period accumulation of the design precipitation sequence. Fig. 13e and c show the spatial distribution of the MP scenario for the drainage areas of Bonneville Dam and Libby Dam, respectively. Fig. 13 shows that the proposed approach can produce the extreme precipitation scenario not only over target drainage areas but over the whole modeling domain, based on the mutual dependency of meteorological/hydrological conditions of the dam systems over the domain. The maximization of each historical AR event increases the cumulative precipitation depths without significantly changing the precipitation distribution pattern over the CRB. The optimization for Bonneville

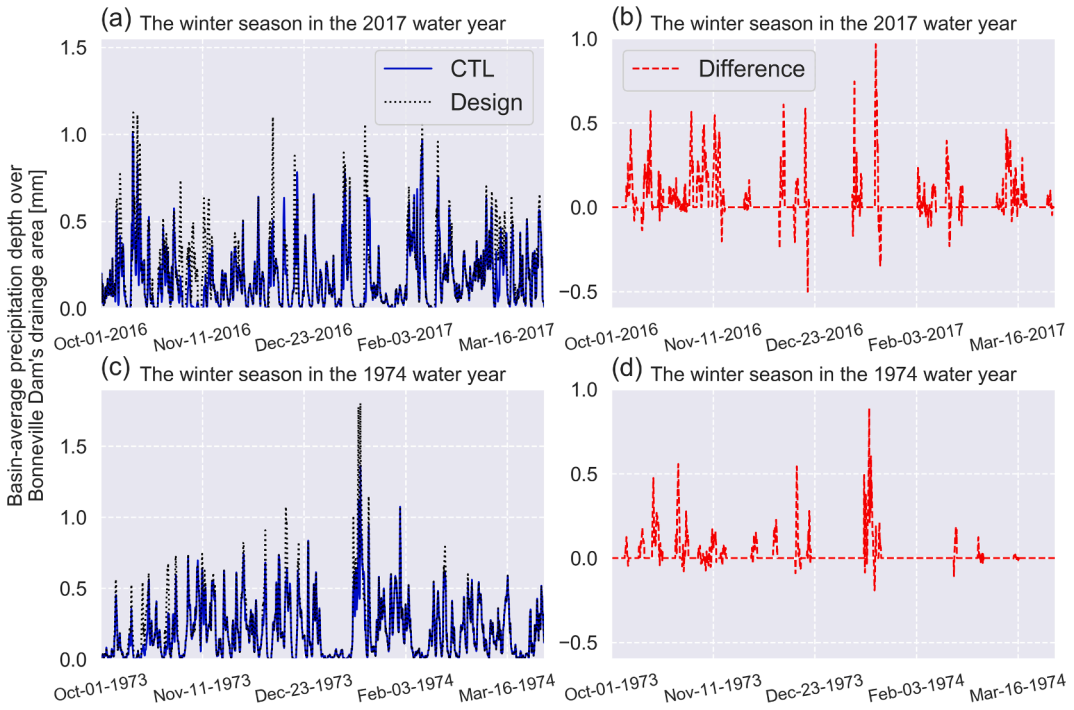

Fig. 9. The design basin-average precipitation sequence (Design) with the basin-average precipitation sequence obtained by the control simulation (CTL) over Bonneville Dam's drainage area during the winter season in the (a) 2017 water year and (c) 1974 water year, and the difference between Design and CTL in the (b) 2017 water year and (d) 1974 water year.

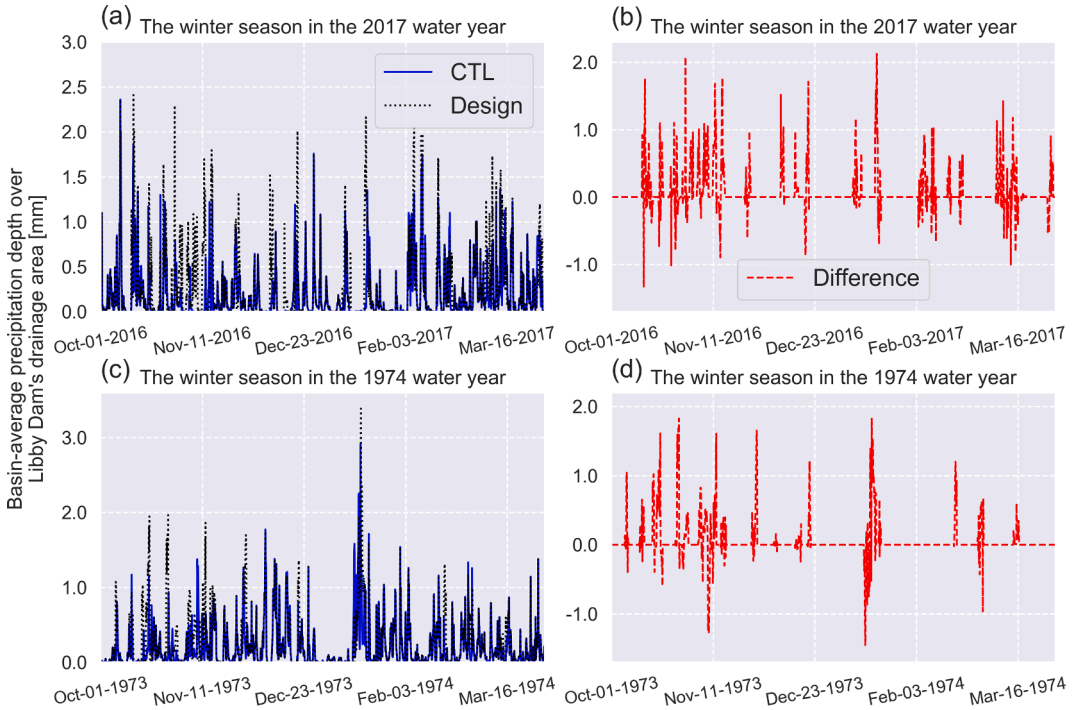

Fig. 10. The design basin-average precipitation sequence (Design) with the basin-average precipitation sequence obtained by the control simulation (CTL) over Libby Dam's drainage area during the winter season in the (a) 2017 water year and (c) 1974 water year, and the difference between Design and CTL during the winter season in the (b) 2017 water year and (d) 1974 water year.

Dam's drainage area intensifies the cumulative precipitation depths, especially at the southern central CRB, where it reaches greater than 2000 mm (Fig. 13b and e). The optimization for Libby Dam's drainage area specifically increases the precipitation depths at the northern CRB (Fig. 13c and f). As a result of optimizing each AR position and RH based on the target basins' terrain characteristics, the cumulative precipitation depth also shows various spatial distributions depending on the target basin.

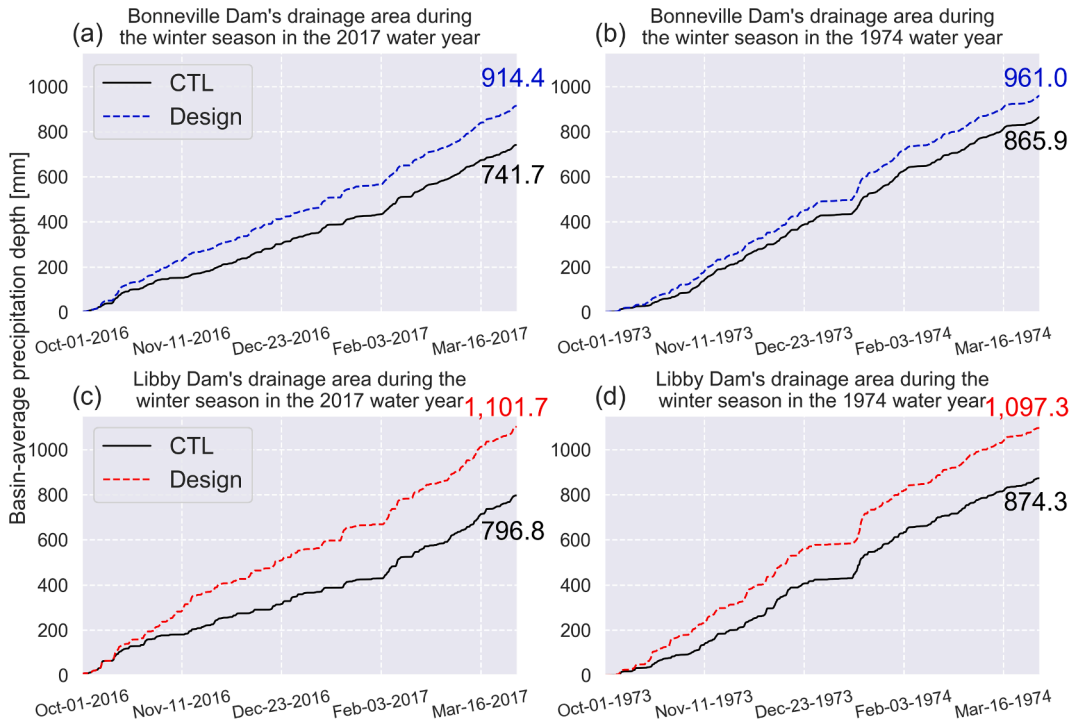

Fig. 11. The cumulative curve of the design basin-average precipitation sequence (Design) with the one of the control simulation (CTL) over (a) Bonneville Dam's drainage area during the winter season in the 2017 water year; (b) Bonneville Dam's drainage area during the winter season in the 1974 water year; (c) Libby Dam's drainage area during the winter season in the 2017 water year; and (d) Libby Dam's drainage area during the winter season in the 1974 water year.

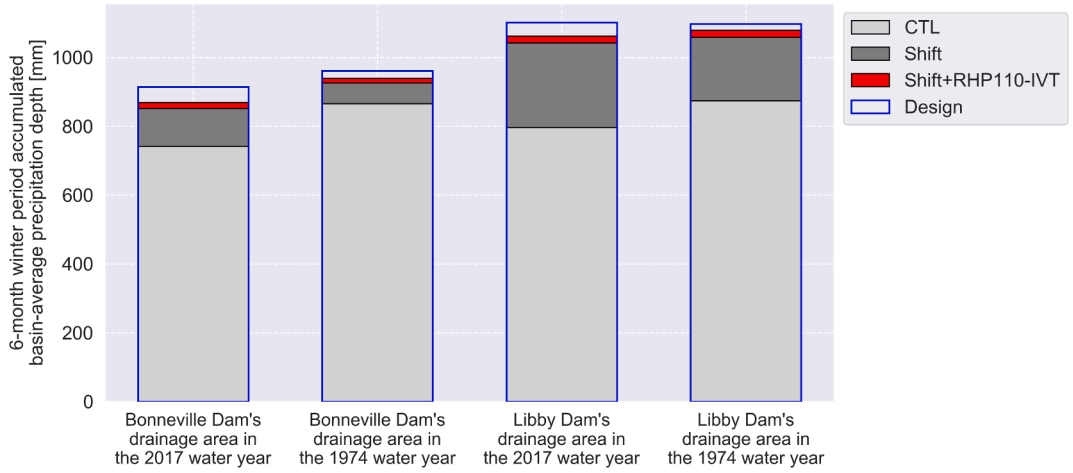

Fig. 12. The 6-month winter period accumulated basin-average precipitation depths over the drainage areas of Bonneville Dam and Libby Dam in the 1974 and 2017 water years. The results obtained by the control simulation (CTL), latitudinal shifting alone (Shift), Shift + RHP110-IVT experiment (Shift + RHP110-IVT), and accumulation of the design precipitation sequence (Design) are shown.

5. Discussion and conclusion

5.1. Identification and maximization of the historical Atmospheric River events

This study identified the hazardous AR events by applying the AR category scale (Ralph et al., 2019) to the entire CRB.. All the identified AR events were then maximized by optimizing the AR position and atmospheric moisture as in Toride et al. (2019). As can be seen from Fig. 8, the maximization of each AR event shows that the basin-average precipitation depth does not necessarily increase with atmospheric moisture, which is consistent with the findings of other recent studies (Ohara et al., 2017; Yang and Smith, 2018). Fig. S3 and S4 show that the change in PW and the change in precipitation depths due to the precipitation maximization are not necessarily consistent, which agrees with the finding of Rastogi et al. (2017). Furthermore, the AR events with higher precipitation depths in the control simulation do not always provide greater increases in precipitation by optimization (Figs. 4 and 5), which is also in agreement with the recent studies by Ishida et al. (2015a,b), Toride et al. (2019).

Our analyses on the AR event maximization show that the precipitation maximization process is grounded in the non-linear relationships among AR position and direction, atmospheric moisture content, and the target basin's geographical characteristics. For instance, Fig. 7 shows that the cumulative basin-average precipitation depth during the AR event 12-b over Libby Dam's drainage area is maximized by 4.9° south

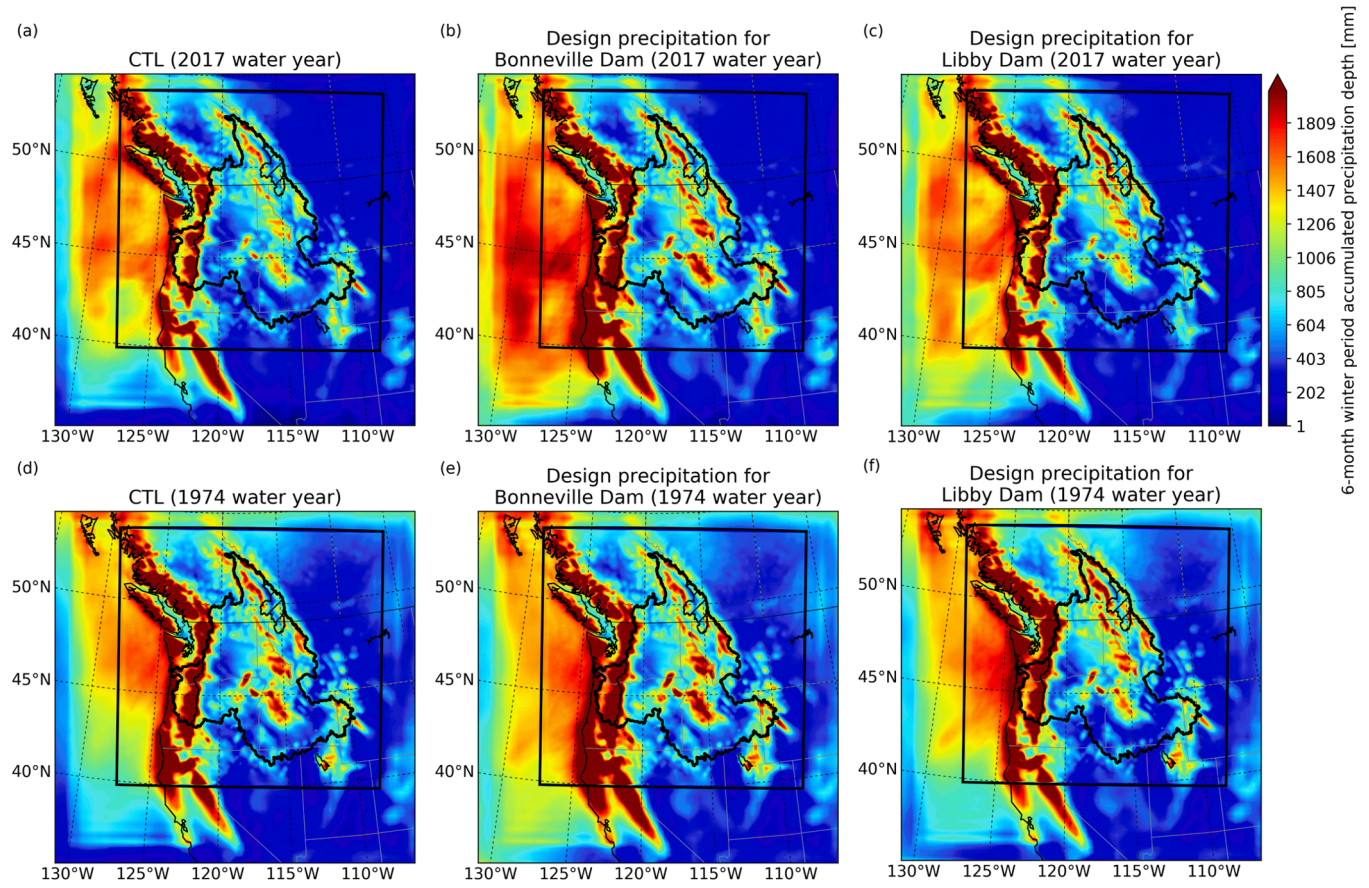

Fig. 13. The spatial distribution of the 6-month winter period accumulated precipitation depths, obtained by (a) the control simulation (CTL) in the 2017 water year; (b) the accumulation of the design precipitation for Bonneville Dam's drainage area in the 2017 water year; (c) the accumulation of the design precipitation for Libby Dam's drainage area in the 2017 water year; (d) the control simulation (CTL) in the 1974 water year; (e) the accumulation of the design precipitation for Bonneville Dam's drainage area in the 1974 water year; and (f) the accumulation of the design precipitation for Libby Dam's drainage area in the 1974 water year.

shifting and RHP100-IVT (Fig. 7f). Nevertheless, its corresponding IVT intensity (Fig. 7c) overall is lower than the IVT intensity obtained by 5.0° south shifting and RHP150-IVT (Fig. 7b). We could interpret this result as follows: When the atmospheric moisture is significantly increased at the boundary where IVT $\geq$ 250 kg m^{-1} s^{-1} by the RHP150-IVT method, as in the AR maximization for Bonneville Dam's drainage area (Fig. 7b and e), the atmosphere can saturate more quickly after injecting the moisture into the domain. This relatively immediate saturation causes heavy precipitation near the boundary where RH is increased. Fig. 7e shows that heavy precipitation occurs around the south-west boundary during the AR event 12-b that enters the modeling domain from the south-west. Meanwhile, this AR event losing some amount of water vapor due to heavy precipitation near the boundary, cannot cause substantial precipitation to the basin far from the boundary unless it attains additional moisture. This immediate saturation process could impact the precipitation depths over Libby Dam's drainage area less since that is located at the north-east of the modeling domain, which is the opposite direction of the boundary where RH was increased.

Meanwhile, the moisture depletion process due to the terrain of the Cascade Range could be a more important factor for determining the contribution of ARs to the precipitation depth over the upper inland basins, such as Libby Dam's drainage area. ARs impacting the upper basins must have a trajectory that favors the IVT penetrating inland through mountain range gaps, or the AR IVT being sufficiently strong and deep (Rutz et al., 2015). Therefore, not only the distance between the boundary and target basin but also the AR trajectories or Cascade Range's elevation should be investigated in order to explain the mechanism of the AR-induced precipitation maximization process. Investigation of this matter further is beyond the scope of this paper. Fig. 8d also shows that the precipitation maximization process is grounded in the aforementioned non-linear relationships between the nature of the AR and terrain characteristics since the relationship between the precipitation depth and RH gradually becomes reversed when the AR is transposed farther south. Similarly, Yang and Smith (2018) reported that extreme rainfall does not show a monotonic increase with atmospheric moisture but also depends upon the pre-storm conditions and complex terrain. Although investigation of the relationship between the landfalling AR nature and terrain characteristics of the target basin is outside the scope of this paper, these findings highlight the importance of the NWM-based approach, which can account for the orographic uplifting effect, moisture convergence, and nonlinearity of the atmosphere, as several studies have asserted (Abbs, 1999; Chen et al., 2017; Ohara et al., 2011).

5.2. Development of the MP estimation for the 6-month winter period

We substituted each historical AR event with its corresponding maximized AR event to form the design precipitation sequence during the winter season, which acts as the basis of the long-duration MP. This sequencing process is based on the concept of the similar process substitution method (WMO, 2009). While the similar process substitution method temporally substitutes some historical storms with different historical storms to form a new precipitation sequence, the proposed method forms a precipitation sequence by maximizing historical AR events in a target water year without combining different storms. In fact, Fig. 11 shows that the cumulative design precipitation depths increase

with time while maintaining an increasing trend over the control simulation's results. This indicates that the proposed method can maximize long-duration cumulative precipitation depths based on the maximization of "historical" AR events over the target basin, rather than creating and introducing "new" AR events to the basin. Besides, as shown in Figs. 11 and 12, a water year with higher precipitation depth in the control simulation does not always provide greater increase in a 6-month accumulated precipitation depth by the maximization process. Although the 1974 water year shows 77.5 mm larger 6-month winter period basin-average precipitation depth over Libby Dam's drainage area than the 2017 water year in the control simulation, the 2017 water year reaches greater precipitation depth as a result of the maximization. This finding is in agreement with the studies by Ishida et al. (2015a,b), Toride et al. (2019) clarifying that the maximization of the storm event with the largest historical precipitation depth does not necessarily yield the MP for a specified duration. It is also in the agreement with Toride et al. (2019) that the latitudinal shifting accounts for the significant part of the increase in the basin-average precipitation depth as shown in Fig. 12.

To the authors' knowledge, this is the first study that estimates the MP for long durations on the order of several months. It should be noted that we define the long-duration MP as a maximum cumulative precipitation depth during a certain time period including several intervals between AR events. Thus, it cannot be simply compared with the MP value estimated in previous studies which focused on a continuous single-storm period (Ishida et al., 2015a, 2015b), in the same context. It is of considerable importance, however, to estimate extreme precipitation series for such a long period in order to assess the role of large hydraulic structures in controlling extreme floods over a target basin, especially in snowmelt-driven regions.

This study estimated the long-duration MP for the very large drainage area of Bonneville Dam which is located at the most downstream of many upstream dam systems in the basin, without treating those dam systems independently, as shown in Fig. 13. In fact, the proposed approach can maximize precipitation depths for different drainage areas within the same large basin by maximizing the same historical AR events, namely, without independently identifying AR events for each drainage area. This is because the proposed approach identifies AR events using the thresholds of IVT over the large basin in which target drainage areas are located. This is one of the most significant advantages of the proposed method from an engineering perspective.

5.3. Limitations and future directions

There are some limitations to this study. First, this study estimates the MP for the 6-month winter period based on only two water years (1974 and 2017) since the primary purpose of this study was to propose a framework to estimate the MP for long durations. However, a more rigorous estimate of the long-duration MP for the target basin could be founded on the consideration of more historical water years. Second, the AR event identification method using the IVT thresholds still has room for improvement. For instance, it might be possible to distinguish different AR systems more rigorously by analyzing the trajectory pathways of the ARs in the identification process. Understanding the trajectory pathways of ARs might lead to a more efficient determination of the atmospheric BC shifting amount as well. However, the simplicity with which the AR events could be identified using only thresholds of IVT over the CRB is one of the strengths of the proposed method. Hence, there is room for consideration as to how much detail is necessary to distinguish the AR events for estimating the long-duration MP. Third, the proposed approach only modified the AR position and atmospheric moisture to maximize precipitation depths during AR events over the CRB, assuming that these modifications can yield extreme precipitation as in the previous studies. However, it might be worth considering the effect of other variables, such as temperature, on the increase in precipitation. There have been some studies revealing the strong relationship between extreme precipitation and other atmospheric variables. Ishida et al. (2018a), Ishida et al. (2018b) found a monotonous increase in the maximum 72-h basin-average precipitation with air temperature over the American River watershed in California. Ohara et al. (2017) examined the optimal wind direction for the extreme storm events to maximize the precipitation over the Feather and American River watersheds. Ben Alaya et al. (2020) found that, using the bivariate extreme value model of PW and precipitation efficiency, the PMP on the North American continental scale increases at a rate of approximately 4% per 1 °C warming. Therefore, it is crucial to investigate the sensitivity of other variables to the increase in precipitation depth and determine which variables to focus on. The modification of atmospheric variables should be sufficiently evaluated not to render the atmospheric system unrealistic.

Future work should expand the proposed framework to other regions where other atmospheric phenomena are dominant in causing severe precipitation. For instance, to expand the proposed framework to the regions where tropical cyclones or hurricanes are dominant, it would be necessary to modify the event identification method and RH perturbation method. Other recent studies (Mure-Ravaud et al., 2019b, 2019a) which investigated the extreme precipitation induced by tropical cyclones or hurricanes using the NWM-approach, could be a good basis for expanding the proposed framework. Moreover, it would be of great interest to estimate the long-duration MP under changing climate. Since the proposed framework identifies AR events based on IVT values calculated by the historical reanalysis datasets, the long-duration MP estimation under future climate scenarios can be developed using the downscaled global circulation model future climate projections (Ishida et al., 2018a, 2018b; Rastogi et al., 2017). It also should be noted that the primary purpose of this effort, the MP estimation during the winter season is toward development of a PMP scenario during the winter and spring season which will be used to calculate a PMF for the target drainage areas (WMO, 2009). The MP estimation during the spring season will be addressed in the second part of an ongoing two-part effort to develop the PMP estimation during the winter and spring seasons. Hence, PMF estimation based on the proposed framework is one significant remaining issue. The proposed NWM-based approach produces not only the precipitation sequence but also other meteorological variables' sequences such as temperature, solar radiation, or wind vector, maintaining the physical relationships with precipitation fields. Thus, a rigorous PMF estimation during the winter and spring seasons could be developed by the hydrological analysis using the meteorological variables obtained by the proposed approach as input data. Gangrade et al. (2018) successfully estimated the PMF over the Alabama-Coosa-Tallapoosa River Basin by conducting hydrological simulation under the 72-hr PMP scenario which was estimated using the RHM method although their analysis did not include snowmelt. Further studies regarding the methodologies for the long-duration MP estimation, such as on methods for improving the event identification or sequencing method, may also be desirable.

CRediT authorship contribution statement

Yusuke Hiraga: Conceptualization, Methodology, Formal analysis, Investigation, Visualization, Writing - original draft. **Yoshihiko Iseri:** Conceptualization, Methodology, Validation, Investigation, Data curation, Visualization, Writing - review & editing. **Michael D. Warner:** Conceptualization, Methodology, Writing - review & editing. **Chris D. Frans:** Conceptualization, Writing - review & editing. **Angela M. Duren:** Conceptualization, Writing - review & editing, Project administration. **John F. England:** Conceptualization, Writing - review & editing. **M. Levent Kavvas:** Conceptualization, Supervision, Project administration, Funding acquisition, Writing - review & editing.

Declaration of Competing Interest

The authors declare that they have no known competing financial interests or personal relationships that could have appeared to influence the work reported in this paper.

Acknowledgements

We thank the editor and three anonymous reviewers for their insightful and constructive comments. This study was supported by U.S. Army Corps of Engineers (USACE) Grant 3-20B35-Department of Army Engi-W912HZ-17-2-0001. The CFSR dataset (ds093.0, doi: 10.5065/D69K487J for 1979 to 2010, ds094.0, doi: 10.5065/D61C1TXF for 2011 to present), and the 20CRv2c dataset (ds131.2, doi: 10.5065/D6N877TW) were obtained through the NCAR/UCAR Research Data Archive. The PRISM dataset is obtained from the PRISM Climate Group (http://www.prism.oregonstate.edu/).

Appendix A. Supplementary data

Supplementary data to this article can be found online at https://doi.org/10.1016/j.jhydrol.2021.126224.

References

Abbs, D.J., 1999. A numerical modeling study to investigate the assumptions used in the calculation of probable maximum precipitation. Water Resour. Res. 35 (3), 785–796. https://doi.org/10.1029/1998WR900013.

Barth, N.A., Villarini, G., Nayak, M.A., White, K., 2017. Mixed populations and annual flood frequency estimates in the western United States: the role of atmospheric rivers. Water Resour. Res. 53 (1), 257–269. https://doi.org/10.1002/2016WR019064.

Beauchamp, J., Leconte, R., Trudel, M., Brissette, F., 2013. Estimation of the summer-fall PMP and PMF of a northern watershed under a changed climate. Water Resour. Res. 49 (6), 3852–3862. https://doi.org/10.1002/wrcr.20336.

Ben Alaya, M.A., Zwiers, F.W., Zhang, X., 2020. Probable maximum precipitation in a warming climate over North America in CanRCM4 and CRCM5. Clim. Change 158 (3-4), 611–629. https://doi.org/10.1007/s10584-019-02591-7.

Casas, M.C., Rodríguez, R., Nieto, R., Redaño, A., 2008. The estimation of probable maximum precipitation: the case of Catalonia. Ann. N. Y. Acad. Sci. 1146, 291–302. https://doi.org/10.1196/annals.1446.003.

Chen, T.C., 1985. Global water wapor flux and Maintenance during FGGE. Mon. Weather Rev. 113, 1801–1819. https://doi.org/10.1175/15200493(1985)113<1801:GWVFAM>2.0.CO;2.

Chen, L.C., Bradley, A.A., 2006. Adequacy of using surface humidity to estimate atmospheric moisture availability for probable maximum precipitation. Water Resour. Res. 42, 1–17. https://doi.org/10.1029/2005WR004469.

Chen, X., Hossain, F., Leung, L.R., 2017. Probable maximum precipitation in the U.S. Pacific Northwest in a Changing Climate. Water Resour. Res. 53 (11), 9600–9622. https://doi.org/10.1002/2017WR021094.

Cheng, L., Aghakouchak, A., 2014. Nonstationary precipitation intensity-duration-frequency curves for infrastructure design in a changing climate. Sci. Rep. 4, 1–6. https://doi.org/10.1038/srep07093.

Chow, V.T., 1951. A general formula for hydrologic frequency analysis. Trans. Am. Geophys. Union. 32 (2), 231. https://doi.org/10.1029/TR032i002p00231.

Cohen, S.J., Miller, K.A., Hamlet, A.F., Avis, W., 2000. Climate change and resource management in the Columbia river basin. Water Int. 25 (2), 253–272. https://doi.org/10.1080/02508060008686827.

Compo, G.P., Whitaker, J.S., Sardeshmukh, P.D., Matsui, N., Allan, R.J., Yin, X., Gleason, B.E., Vose, R.S., Rutledge, G., Bessemoulin, P., Brönnimann, S., Brunet, M., Crouthamel, R.I., Grant, A.N., Groisman, P.Y., Jones, P.D., Kruk, M.C., Kruger, A.C., Marshall, G.J., Maugeri, M., Mok, H.Y., Nordli, Ø., Ross, T.F., Trigo, R.M., Wang, X. L., Woodruff, S.D., Worley, S.J., 2011. The twentieth century reanalysis project. Q. J. R. Meteorol. Soc. 137 (654), 1–28. https://doi.org/10.1002/qj.776.

Daly, C., Halbleib, M., Smith, J.I., Gibson, W.P., Doggett, M.K., Taylor, G.H., Curtis, J., Pasteris, P.P., 2008. Physiographically sensitive mapping of climatological temperature and precipitation across the conterminous United States. Int. J. Climatol. 28 (15), 2031–2064. https://doi.org/10.1002/joc.v28:1510.1002/joc.1688.

Desa M, M.N., Noriah, A.B., Rakhecha, P.R., 2001. Probable maximum precipitation for 24h duration over southeast Asian monsoon region – Selangor, Malaysia. Atmos. Res. 58 (1), 41–54. https://doi.org/10.1016/S0169-8095(01)00070-9.

Ek, M.B., Mitchell, K.E., Lin, Y., Rogers, E., Grunmann, P., Koren, V., Gayno, G., Tarpley, J.D., 2003. Implementation of Noah land surface model advances in the National Centers for Environmental Prediction operational mesoscale Eta model. J. Geophys. Res. D Atmos. 108, 1–16. https://doi.org/10.1029/2002jd003296.

Flores, T., Griffith, S., 2002. Portland Flood, 1894 [WWW Document]. Oregon Hist. Proj. URL https://oregonhistoryproject.org/articles/historical-records/portland-flood-1894/.

Gangrade, S., Kao, S.-C., Naz, B.S., Rastogi, D., Ashfaq, M., Singh, N., Preston, B.L., 2018. Sensitivity of probable maximum flood in a changing environment. Water Resour. Res. 54 (6), 3913–3936. https://doi.org/10.1029/2017WR021987.

Gao, M., Mo, D., Wu, X., 2016. Nonstationary modeling of extreme precipitation in China. Atmos. Res. 182, 1–9. https://doi.org/10.1016/j.atmosres.2016.07.014.

Hamlet, A.F., Lettenmaier, D.P., 1999. Effects of climate change on hydrology and water resources in the Columbia River Basin. J. Am. Water Resour. Assoc. 35 (6), 1597–1623. https://doi.org/10.1111/j.1752-1688.1999.tb04240.x.

Hansen, E.M., Schreiner, L.C., Miller, J.F., 1982. Application of probable maximum precipitation estimates – United States east of the 105th meridian. NWS Hydrometeorological Rep. 52, 182. https://www.nws.noaa.gov/oh/hdsc/PMP_documents/HMR52.pdf.

Hansen, E.M., Fenn, D.D., Corrigan, P., Vogel, J.L., Schreiner, L.C., Stodt, R.W., 1994. Probable maximum precipitation -Pacific Northwest states: Columbia River (including portions of Canada), Snake River and Pacific coastal drainages. NWS Hydrometeorological Rep. 57, 353. https://www.nws.noaa.gov/oh/hdsc/PMP_documents/HMR57.pdf.

Hershfield, D.M., 1961. Estimating the probable maximum precipitation. J. Hydraul. Div. 87 (5), 99–116.

Hershfield, D.M., 1965. Method for estimating probable maximum rainfall. J. Am. Water Works Assoc. 57 (8), 965–972. https://doi.org/10.1002/j.1551-8833.1965.tb01486.x.

Iacono, M.J., Delamere, J.S., Mlawer, E.J., Shephard, M.W., Clough, S.A., Collins, W.D., 2008. Radiative forcing by long-lived greenhouse gases: calculations with the AER radiative transfer models. J. Geophys. Res. Atmos. 113, 2–9. https://doi.org/10.1029/2008JD009944.

Ishida, K., Kavvas, M.L., Chen, Z.Q.R., Dib, A., Diaz, A.J., Anderson, M.L., Trinh, T., 2018a. Physically based maximum precipitation estimation under future climate change conditions. Hydrol. Process. 32 (20), 3188–3201. https://doi.org/10.1002/hyp.13253.

Ishida, K., Kavvas, M.L., Jang, S., Chen, Z.Q., Ohara, N., Anderson, M.L., 2015a. Physically based estimation of maximum precipitation over three watersheds in Northern California: atmospheric boundary condition shifting. J. Hydrol. Eng. 20 (4), 04014052. https://doi.org/10.1061/(ASCE)HE.1943-5584.0001026.

Ishida, K., Kavvas, M.L., Jang, S., Chen, Z.Q., Ohara, N., Anderson, M.L., 2015b. Physically based estimation of maximum precipitation over three watersheds in Northern California: relative humidity maximization method. J. Hydrol. Eng. 20 (10) https://doi.org/10.1061/(ASCE)HE.1943-5584.0001175, 04015014.

Ishida, K., Ohara, N., Kavvas, M.L., Chen, Z.Q., Anderson, M.L., 2018b. Impact of air temperature on physically-based maximum precipitation estimation through change in moisture holding capacity of air. J. Hydrol. 556, 1050–1063. https://doi.org/10.1016/j.jhydrol.2016.10.008.

Janjić, Z.I., 1994. The Step-mountain eta coordinate model: further developments of the convection, viscous sublayer, and turbulence closure schemes. Mon. Weather Rev. 122, 927–945. https://doi.org/10.1175/1520-0493(1994)122b0927:TSMECMN2.0.CO;2.

Knippertz, P., Wernli, H., 2010. A lagrangian climatology of tropical moisture exports to the northern hemispheric extratropics. J. Clim. 23, 987–1003. https://doi.org/10.1175/2009JCLI3333.1.

Koutsoyiannis, D., 1999. A probabilistic view of Hershfield's method for estimating probable maximum precipitation. Water Resour. Res. 35 (4), 1313–1322. https://doi.org/10.1029/1999WR900002.

Kunkel, K.E., Karl, T.R., Easterling, D.R., Redmond, K., Young, J., Yin, X., Hennon, P., 2013. Probable maximum precipitation and climate change. Geophys. Res. Lett. 40 (7), 1402–1408. https://doi.org/10.1002/grl.50334.

Lee, S.-Y., Hamlet, A.F., Fitzgerald, C.J., Burges, S.J., Lettenmaier, D.P., 2009. Optimized flood control in the Columbia River Basin for a global warming scenario. J. Water Resour. Plann. Manage. 135, 440–450. https://doi.org/10.1061/(ASCE)0733-9496(2009)135:6(440).

Lin, Y., Colle, B.A., 2011. A new bulk microphysical scheme that includes riming intensity and temperature-dependent ice characteristics. Mon. Weather Rev. 139, 1013–1035. https://doi.org/10.1175/2010MWR3293.1.

Liu, T., Liang, Z., Chen, Y., Lei, X., Li, B., 2018. Long-duration PMP and PMF estimation with SWAT model for the sparsely gauged Upper Nujiang River Basin. Nat. Hazards 90 (2), 735–755. https://doi.org/10.1007/s11069-017-3068-z.

Martin Ralph, F., Rutz, J.J., Cordeira, J.M., Dettinger, M., Anderson, M., Reynolds, D., Schick, L.J., Smallcomb, C., 2019. A scale to characterize the strength and impacts of atmospheric rivers. Bull. Am. Meteorol. Soc. 100, 269–289. https://doi.org/10.1175/BAMS-D-18-0023.1.

McGregor, M.N., 2003. The Vanport Flood [WWW Document]. Oregon Hist. Proj. URL https://oregonhistoryproject.org/articles/essays/the-vanport-flood/.

Mure-Ravaud, M., Dib, A., Kavvas, M.L., Yegorova, E., Kanney, J., 2019a. Physically based storm transposition of four Atlantic tropical cyclones. Sci. Total Environ. 666, 252–273. https://doi.org/10.1016/j.scitotenv.2019.02.141.

Mure-Ravaud, M., Kavvas, M.L., Dib, A., 2019b. Impact of increased atmospheric moisture on the precipitation depth caused by Hurricane Ivan (2004) over a target area. Sci. Total Environ. 672, 916–926. https://doi.org/10.1016/j.scitotenv.2019.03.471.

National Weather Service, 2019. COLUMBIA RIVER AT VANCOUVER, Advanced Hydrologic Prediction Service. https://water.weather.gov/ahps2/hydrograph.php?gage=vapw1&wfo=pqr (accessed 17 October 2020).

Neiman, P.J., Ralph, F.M., Wick, G.A., Lundquist, J.D., Dettinger, M.D., 2008. Meteorological characteristics and overland precipitation impacts of atmospheric

rivers affecting the West coast of North America based on eight years of SSM/I satellite observations. J. Hydrometeorol. 9, 22–47. https://doi.org/10.1175/2007JHM855.1.
Neiman, P.J., Schick, L.J., Martin Ralph, F., Hughes, M., Wick, G.A., 2011. Flooding in western washington: the connection to atmospheric rivers. J. Hydrometeorol. 12, 1337–1358. https://doi.org/10.1175/2011JHM1358.1.
Nelson, E.R., 1949. Columbia river basin flood. Mon. Weather Rev. 77, 1–10. https://doi.org/10.1175/1520-0493(1949)077<0001:crbf>2.0.co;2.
Newell, R.E., Newell, N.E., Zhu, Y., Scott, C., 1992. Tropospheric rivers?—a pilot study. Geophys. Res. Lett. 19 (24), 2401–2404. https://doi.org/10.1029/92GL02916.
Nobilis, F., Haiden, T., Kerschbaum, M., 1991. Statistical considerations concerning Probable Maximum Precipitation (PMP) in the Alpine Country of Austria. Theor. Appl. Climatol. 44 (2), 89–94. https://doi.org/10.1007/BF00867996.
O'Connor, J. E., Costa, J. E. 2004. The World's Largest Floods, Past and Present: Their Causes and Magnitudes. U.S. Geological Survey Circular 1254, 13. http://pubs.usgs.gov/circ/2004/circ1254/pdf/circ1254.pdf.
Ohara, N., Kavvas, M.L., Anderson, M.L., Chen, Z.Q., Ishida, K., 2017. Characterization of extreme storm events using a numerical model-based precipitation maximization procedure in the feather, Yuba, and American River Watersheds in California. J. Hydrometeorol. 18, 1413–1423. https://doi.org/10.1175/JHM-D-15-0232.1.
Ohara, N., Kavvas, M.L., Kure, S., Chen, Z.Q., Jang, S., Tan, E., 2011. Physically based estimation of maximum precipitation over American River Watershed. California. J. Hydrol. Eng. 16 (4), 351–361. https://doi.org/10.1061/(ASCE)HE.1943-5584.0000324.
Rakhecha, P.R., Deshpande, N.R., Soman, M.K., 1992. Probable maximum precipitation for a 2-day duration over the Indian Peninsula. Theor. Appl. Climatol. 45 (4), 277–283. https://doi.org/10.1007/BF00865518.
Ralph, F.M., Dettinger, M.D., 2012. Historical and national perspectives on extreme west coast precipitation associated with atmospheric rivers during December 2010. Bull. Am. Meteorol. Soc. 93 (6), 783–790. https://doi.org/10.1175/BAMS-D-11-00188.1.
Ralph, F.M., Neiman, P.J., Wick, G.A., 2004. Satellite and CALJET aircraft observations of atmospheric rivers over the Eastern North Pacific Ocean during the winter of 1997/98. Mon. Weather Rev. 132, 1721–1745. https://doi.org/10.1175/1520-0493(2004)132<1721:SACAOO>2.0.CO;2.
Rantz, S. E., Riggs, H. C., 1949. Floods of May–June 1948 in Columbia River Basin – a presentation of data on floods, gathered from selected gaging stations and other sources. Geological Survey Water-Supply Paper 1080, U.S. Government Printing Office Washington.
Rastogi, D., Kao, S.-C., Ashfaq, M., Mei, R., Kabela, E.D., Gangrade, S., Naz, B.S., Preston, B.L., Singh, N., Anantharaj, V.G., 2017. Effects of climate change on probable maximum precipitation: a sensitivity study over the Alabama-Coosa-Tallapoosa River Basin. J. Geophys. Res. 122 (9), 4808–4828. https://doi.org/10.1002/2016JD026001.
Rezacova, D., Pesice, P., Sokol, Z., 2005. An estimation of the probable maximum precipitation for river basins in the Czech Republic. Atmos. Res. 77 (1-4), 407–421. https://doi.org/10.1016/j.atmosres.2004.10.011.
Rouhani, H., Leconte, R., 2016. A novel method to estimate the maximization ratio of the Probable Maximum Precipitation (PMP) using regional climate model output. Water Resour. Res. 52 (9), 7347–7365. https://doi.org/10.1002/2016WR018603.
Rousseau, A.N., Klein, I.M., Freudiger, D., Gagnon, P., Frigon, A., Ratté-Fortin, C., 2014. Development of a methodology to evaluate probable maximum precipitation (PMP) under changing climate conditions: application to southern Quebec. Canada. J. Hydrol. 519, 3094–3109. https://doi.org/10.1016/j.jhydrol.2014.10.053.
Rutz, J.J., James Steenburgh, W., Martin Ralph, F., 2015. The inland penetration of atmospheric rivers over western North America: a Lagrangian analysis. Mon. Weather Rev. 143, 1924–1944. https://doi.org/10.1175/MWR-D-14-00288.1.
Rutz, J.J., James Steenburgh, W., Martin Ralph, F., 2014. Climatological characteristics of atmospheric rivers and their inland penetration over the western united states. Mon. Weather Rev. 142, 905–921. https://doi.org/10.1175/MWR-D-13-00168.1.
Saha, S., Moorthi, S., Pan, H.-L., Wu, X., Wang, J., Nadiga, S., Tripp, P., Kistler, R., Woollen, J., Behringer, D., Liu, H., Stokes, D., Grumbine, R., Gayno, G., Wang, J., Hou, Y.-T., Chuang, H.-ya., Juang, H.-M., Sela, J., Iredell, M., Treadon, R., Kleist, D., Van Delst, P., Keyser, D., Derber, J., Ek, M., Meng, J., Wei, H., Yang, R., Lord, S., van den Dool, H., Kumar, A., Wang, W., Long, C., Chelliah, M., Xue, Y., Huang, B., Schemm, J.-K., Ebisuzaki, W., Lin, R., Xie, P., Chen, M., Zhou, S., Higgins, W., Zou, C.-Z., Liu, Q., Chen, Y., Han, Y., Cucurull, L., Reynolds, R.W., Rutledge, G., Goldberg, M., 2010. The NCEP climate forecast system reanalysis. Bull. Am. Meteorol. Soc. 91 (8), 1015–1058. https://doi.org/10.1175/2010BAMS3001.1.
Sarkar, S., Maity, R., 2020a. Increase in probable maximum precipitation in a changing climate over India. J. Hydrol 585, 124806. https://doi.org/10.1016/j.jhydrol.2020.124806.
Sarkar, S., Maity, R., 2020b. Estimation of probable maximum precipitation in the context of climate change. MethodsX 7, 100904. https://doi.org/10.1016/j.mex.2020.100904.
Sherif, M., Almulla, M., Shetty, A., Chowdhury, R.K., 2014. Analysis of rainfall, PMP and drought in the United Arab Emirates. Int. J. Climatol. 34 (4), 1318–1328. https://doi.org/10.1002/joc.3768.
Skamarock, W.C., Klemp, J.B., Dudhi, J., Gill, D.O., Barker, D.M., Duda, M.G., Huang, X.-Y., Wang, W., Powers, J.G., 2008. A description of the advanced research WRF version 3. Tech. Rep. 113 https://doi.org/10.5065/D6DZ069T.
Stanford, J.A., Gregory, S.V., Hauer, F.R., Snyder, E.B., 2005. ColumbiaRiver basin. In: Benke, A.C., Cushing, C.E. (Eds.), Rivers of NorthAmerica. Elsevier Academic Press, Amsterdam, pp. 591–653.
Tajbakhsh, M., Al-Ansari, N., 2019. Comparative study of multi-station method and Hershfield's approaches for PMP determination (case study: Northeast of Iran). Sustain. Water Resour. Manag. 5 (3), 1133–1141. https://doi.org/10.1007/s40899-018-0291-z.
Toride, K., Iseri, Y., Warner, M.D., Frans, C.D., Duren, A.M., England, J.F., Kavvas, M.L., 2019. Model-based probable maximum precipitation estimation: how to estimate the worst-case scenario induced by atmospheric rivers? J. Hydrometeorol. 20, 2383–2400. https://doi.org/10.1175/JHM-D-19-0039.1.
USACE, 2019. Probable Maximum Precipitations for Columbia Basin Dams. USACE.
U.S. Department of the Interior, Bureau of Reclamation, 2016. SECURE Water Act Section 9503(c) Report to Congress Chapter 4: Columbia River Basin.
U.S. Weather Bureau, 1945. Tentative Estimates of Maximum Possible Flood-Producing Meteorological Conditions in the Columbia River Basin. Hydrometeorological Rep. 18, 1-2. https://www.weather.gov/media/owp/oh/hdsc/docs/HMR18.pdf.
Warner, M.D., Mass, C.F., Salatheé, E.P., 2012. Wintertime extreme precipitation events along the Pacific Northwest Coast: climatology and synoptic evolution. Mon. Weather Rev. 140, 2021–2043. https://doi.org/10.1175/MWR-D-11-00197.1.
Willingham, B.W.F., 2014. Willamette River flood of 1894 [WWW Document]. Oregon Encycl. URL https://oregonencyclopedia.org/articles/willamette_flood_1894_/.
World Meteorological Organization (WMO), 2009. Manual on estimation of Probable Maximum Precipitation (PMP), WMO-No. 1045, https://library.wmo.int/doc_num.php?explnum_id57706.
Yang, L., Smith, J., 2018. Sensitivity of extreme rainfall to atmospheric moisture content in the arid/semiarid Southwestern United States: implications for probable maximum precipitation estimates. J. Geophys. Res. Atmos. 123 (3), 1638–1656. https://doi.org/10.1002/2017JD027850.
Zhang, G.J., McFarlane, N.A., 1995. Sensitivity of climate simulations to the parameterization of cumulus convection in the canadian climate centre general circulation model. Atmos. – Ocean 33 (3), 407–446. https://doi.org/10.1080/07055900.1995.9649539.
Zhao, W., Smith, J.A., Bradley, A.A., 1997. Numerical simulation of a heavy rainfall event during the PRE-STORM experiment. Water Resour. Res. 33 (4), 783–799. https://doi.org/10.1029/96WR03036.
Zhu, Y., Newell, R.E., 1998. A proposed algorithm for moisture fluxes from atmospheric rivers. Mon. Weather Rev. 126, 725–735. https://doi.org/10.1175/1520-0493(1998)126<0725:APAFMF>2.0.CO;2.